

Cesium atoms in a cryogenic argon matrix

T. Battard ¹, S. Lahs ¹, C. Crépin ² and D. Comparat ^{1,*}

¹*Université Paris-Saclay, CNRS, Laboratoire Aimé Cotton, 91405 Orsay, France*

²*Université Paris-Saclay, CNRS, Institut des Sciences Moléculaires d'Orsay, 91405 Orsay, France*



(Received 11 May 2023; accepted 18 September 2023; published 26 October 2023)

This paper presents both experimental and theoretical investigations into the spectroscopy of dilute cesium (Cs) atoms within a solid argon (Ar) matrix at cryogenic temperatures. This system is relevant for matrix isolation spectroscopy and in particular for recently proposed methods for investigating phenomena that extend beyond the standard model of particle physics. We record absorption spectra at various deposition temperatures and examine the evolution of these spectra after deposition with respect to temperature changes. Taking advantage of Cs-Ar and Ar-Ar pairwise interaction potentials, we conduct a stability study of trapping sites, which indicates a preference for T_d (tetrahedral, four vacancies) and O_h (cubic, six vacancies) symmetries. By implementing a mean-field analysis of the long-range Cs($6s$, $6p$)-Ar-Ar triple dipole interaction, combined with a temperature-dependent shift in zero-point energy, we propose effective Cs($6s$, $6p$)-Ar pairwise potentials. Upon integrating these pairwise potentials with spin-orbit coupling, we achieve a satisfactory agreement between the observed and simulated absorption line positions. The observed line broadening is reasonably well reproduced by a semiclassical thermal Monte Carlo approach based on Mulliken-type differences between excited and ground potential curves. Additionally, we develop a simple, first-order crystal-field theory featuring only six interaction mode coordinates. It uses the reflection approximation and incorporates quantized (phonon) normal modes. This produces a narrow triplet structure but not the observed amount of splitting.

DOI: [10.1103/PhysRevA.108.042820](https://doi.org/10.1103/PhysRevA.108.042820)

I. INTRODUCTION

Despite matrix isolation spectroscopy having been studied since the 1950s [1–3], our understanding of the shape and behavior of trapping environments within the matrix remains limited. This is particularly true for even the simplest systems comprising single valence electron atoms (alkali-metal atoms) in rare gas matrix environments, where no consensus has yet been reached regarding the trapping site with the host atom, especially for heavier atoms [4–6].

Gaining a more accurate understanding of the trapping site and the matrix's effect on the dopant would prove invaluable for precision spectroscopy experiments, such as magnetometry, spin-dependent interactions, and investigations into physics beyond the Standard Model. These investigations may include searches for violations of fundamental symmetries (parity, time-reversal) like electric dipole moment (EDM) in particles or axion-like dark matter candidates. Precision spectroscopy experiments utilize spin-induced transitions, which are not directly affected by the matrix's pure electrostatic interaction at first order. However, a detailed study is necessary to assess the precision that these experiments can attain [7–13].

In this article, our focus is on studying cesium atoms trapped in an argon matrix. Understanding this simple system will help to further characterize more complex experiments.

Among the (stable) alkali-metal atoms, cesium is the heaviest, making it highly sensitive to the effects of the electron EDM [14]. We have chosen argon because it is the only rare gas whose naturally occurring isotopes do not possess a nuclear spin that would interact with the cesium spin.

Absorption (or transmission) spectra form the foundation for all optical manipulations necessary for the above-proposed experiments. Intriguingly, only a few experiments have studied Cs embedded in Ar [15,16], and only two optical transmission spectra have been published [17,18] ([19] gives only absorption and emission frequencies). For Cs in Ar, two structures were observed. They could arise from $6s \rightarrow 6p$ transitions in two different trapping site environments: the $6p$ triplet degeneracy being lifted either by a low symmetry site [17] or by a dynamical Jahn-Teller effect in a cubic symmetry site [18]. Reference [19] observed, in addition, $6s \rightarrow 5d$ and $6s \rightarrow 7p$ transitions, along with relaxation and fluorescence from $6p$ and $5d$ levels.

In this article, we conduct experiments with the aim of reconciling the discrepancies between previous measurements. We begin by presenting the experimental setup, which enables precise Cs density measurements in highly polycrystalline Ar samples. Then, using Cs-Ar and Ar-Ar pairwise interaction potentials, we first conduct a trapping site stability study. By correcting the pairwise interaction with effective third-order effects, we predict absorption line positions for the different trapping sites found. We then validate, using a simple crystal-field model, whether the found linewidths agrees with the proposed trapping sites. Finally, we provide conclusions and potential improvements for further exploration.

*Corresponding author: daniel.comparat@universite-paris-saclay.fr

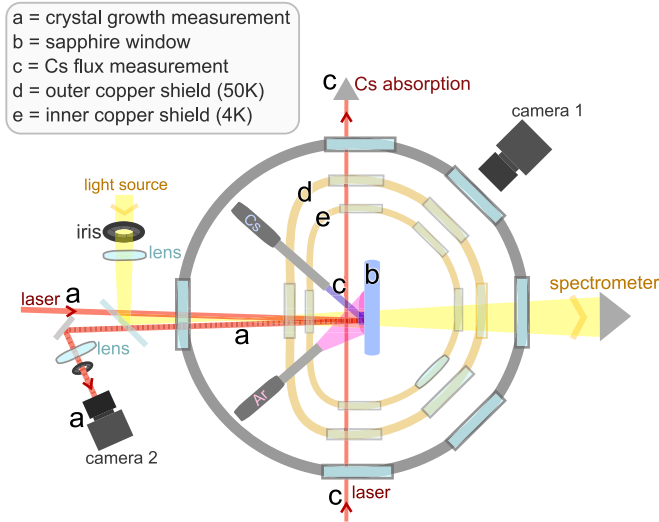


FIG. 1. Schematic representation of the cryostat and the optical systems utilized to monitor the matrix growth rate and to measure the absorption and fluorescence spectra. The arrows indicate the propagation directions of the beams. The laser illumination of the matrix is imaged on CCD camera 2 to display the interference pattern.

II. EXPERIMENTAL SETUP

Figure 1 illustrates the experimental setup. The experiment is performed under a residual gas pressure of $\sim 10^{-7}$ mbar in a two-stage cryostat manufactured by Mycryofirm using a pulsed tube cryocooler (SHI RP-082E2S). The cryogenic matrix is grown by depositing Ar gas onto a C-cut sapphire (Al_2O_3) plate, which is 20 mm in diameter and 1 mm in thickness, and embedded in a copper frame. The cryogenic temperature of the sample holder, ranging from 3 K to 30 K, is regulated via resistive heating. In order to minimize thermal disturbances caused by the kinetic energy transfer of the Ar beam, the sample holder's temperature is maintained at a constant level via a PID loop.

A. Sample growth

The thickness L of the argon layer is continuously monitored via 2D reflection Fizeau interferometry. A pattern formed by the interference between the light reflected from the front and back sides of the matrix is captured by a lens onto a CCD camera. The 2D imaging offers numerous advantages compared to previous 1D transmission or reflection laser interferometry studies [20–22]: it features a background-free environment ensuring excellent contrast, it is less restricted by beam size and spatial interference narrowing, and it enables the monitoring of the whole sample thereby ensuring the quality of deposition.

For this Ar growth measurement, a DFB diode laser operating at $\lambda = 852$ nm was employed, providing the advantage of also allowing the monitoring of the Cs flux through saturated absorption.

The interference fringes at a specific point evolve as per $\frac{2n_{\text{Ar}}}{\lambda} \frac{dL}{dt}$, where $n_{\text{Ar}} = 1.3$ is the refractive index of an argon bulk crystal at 852 nm [23].

A growth of approximately three fringes per minute is observed, corresponding to a growth rate for an ideal argon bulk crystal of $\frac{dL}{dt} = 1 \mu\text{m}/\text{min}$. After about one hour of argon deposition, a crystal is formed with a thickness of $\sim 50 \mu\text{m}$.

B. Cs density

To embed cesium into the matrix, we utilize Alfasource 3S dispensers (Alfavakuo e.U.) loaded with a CsBi_{25} alloy. The dispenser is situated outside the 50 K and 4 K thermal shields and is activated by resistive current heating. The Cs vapor is funneled to the substrate through a steel tube with an inner diameter d of 4 mm, which pierces both thermal shields. Independently, the tube is heated to approximately 40°C via resistors to minimize blockage from condensing Cs. We have extensively studied in Ref. [24] the behavior of cesium atom effusion through a collimating tube and established that, irrespective of the tube material, Cs adheres to the wall. This results in a well-collimated and homogeneous Cs atomic beam.

We monitor the Cs flux by recording a laser absorption spectrum while adjusting the frequency of the low-intensity diode laser intersecting the cesium beam. We assume that the Cs beam diameter aligns with the inner tube diameter d and its density n is uniform. Confirmation of this is obtained by scanning the laser beam through the atomic beam or by a simple 2D absorption image of the Cs in the Ar matrix, where the cesium-doped zone creates a visible spot that is about 5 mm wide. The velocity distribution is effusive [24]: $f_z(v_z) =$

$\left(\frac{m}{\sqrt{2k_B T_z}}\right)^2 v_z^3 e^{-\frac{mv_z^2}{2k_B T_z}}$ along z . The Cs beam is intersected by the laser at an angle of $\alpha = 22^\circ$ relative to the beam axis, as shown in Fig. 1. Hence, the Beer-Lambert-Bouguer absorption is given by $nd\sigma_0 \int_0^\infty \frac{1}{1 + \left(\frac{\omega_L - \omega_{Cs} - kv_z \sin \alpha}{\Gamma/2}\right)^2} f_z(v_z) dv_z$ where

$\sigma_0 = 1.4 \times 10^{-9} \text{ cm}^2$ is the absorption cross section for an isotropic light polarization at the resonant $6s_{1/2}(F=4) \rightarrow 6p_{3/2}(F=5)$ frequency $\hbar\omega_{Cs}$, which has a natural spontaneous decay rate of $\Gamma = 1/(30.4 \text{ ns})$ [25]. We fit the experimental absorption profile to this formula while scanning the laser angular frequency ω_L . The results align with and are not highly sensitive to $T_z \approx 400$ K. We then determine the beam density n and consequently the Cs flux $n\pi(d/2)^2\bar{v}$, where $\bar{v} = \sqrt{8k_B T_z/\pi m}$ is the average velocity. We only account for the population in the hyperfine level $F=4$ (which represents only 9/16 of the total Cs($6s$) population in the beam, assuming Boltzmann-equidistribution between the nine times degenerate $F=4$ and 7 times $F=3$ levels). Ultimately, we obtain a Cs($6s$) flux of a few 10^{12} at/s reaching the Ar matrix. We thus anticipate a $\sim 10^{-4}$ atomic ratio of Cs in the argon matrix (density on the order of 10^{18} cm^{-3}) and a typical average internuclear distance between Cs atoms on the order of 10 nm.

To prevent Cs contamination of the window and to generate well-defined trapping environments for all the Cs atoms, we always initiate Cs deposition only after a few micrometers of Ar have already been deposited.

C. Quality of the samples

Undoubtedly, the epitaxy of an fcc Ar crystal is unfeasible on the hexagonal lattice of sapphire due to the incompatibility

of their structural lattices [26], leading to the formation of several crystal defects, including holes or cavities, as observed in Ref. [26].

In theory, Cs can be trapped in various defect types such as point defects surrounded by vacancies or line-dislocation defects (including screw, edge, etc.), surface defects (like stacking fault, tilt and twist grain boundaries), or volume defects (e.g., pores, cracks, or alternate phases like hcp inclusions) [27].

It is known from literature that the grain size is inversely proportional to the growth rate [28], and the deposition temperature significantly influences the crystal quality. The crystals contain twins, stacking faults, and dislocations [29]. At 20 K and 10 K, the interdislocation distances are roughly 8 nm and 3 nm, respectively [30,31]. This suggests the likely presence of small crystallites comprising thousands of atoms, separated by dislocations. Additionally, if a film is grown at a condensation temperature greater than two thirds of the sublimation temperature (that is 30 K for Ar), the fcc grains are about 100 nm in size. Conversely, at one third of the sublimation temperature (that is about 10 K for Ar), the grain size reduces to around 10 nm, with indications of a minority hcp phase [28,29,32]. Furthermore, below a critical temperature (18 K for Ar), atomic-scale cavities appear in the lattice [33].

These studies align well with our experimental observations regarding the quality of the Fizeau interference image during crystal growth, and the reduction in light transmission intensity due to scattering on grain boundaries. Specifically, as described in [34], a sample turns almost opaque when the Ar crystal grain diameter reaches around 0.1λ . We attribute this to exactly this increased scattering.

Although we attempted annealing up to 30 K, the Ar crystal quality showed no significant improvement. This outcome aligns with expectations, as higher temperatures (closer to the triple point) would be necessary [35,36] to promote vacancy formation or atom-vacancy exchange through diffusion [37–39]. However, achieving such temperatures in a free-standing sample in vacuum is not possible as sublimation would occur prematurely due to the high vapor pressure of solid argon.

III. ABSORPTION SPECTRA

A. Experimental spectra

In our absorption (or transmission) spectroscopy, we use an Avantes AvaLight-HAL tungsten-halogen light source and an Ocean Optics QE65000 spectrometer. The spectrometer was calibrated by measuring the spectra of Hg and Kr lamps.

To measure the absorption in the doped Ar crystal, we shine light from the lamp through the sample. The position and shape of the light on the plate can be adjusted with irises and mirrors and monitored via a camera.

We then compute the spectral absorbance of the sample due to Cs as $A = \log_{10} \frac{I_0}{I_t}$, where I_t denotes the spectral irradiance density recorded in the presence of the Cs-Ar sample, and I_0 is obtained prior to any Cs deposition.

The captured spectra from varying deposition temperatures are presented in Fig. 2(a). Above 14 K, the spectra become

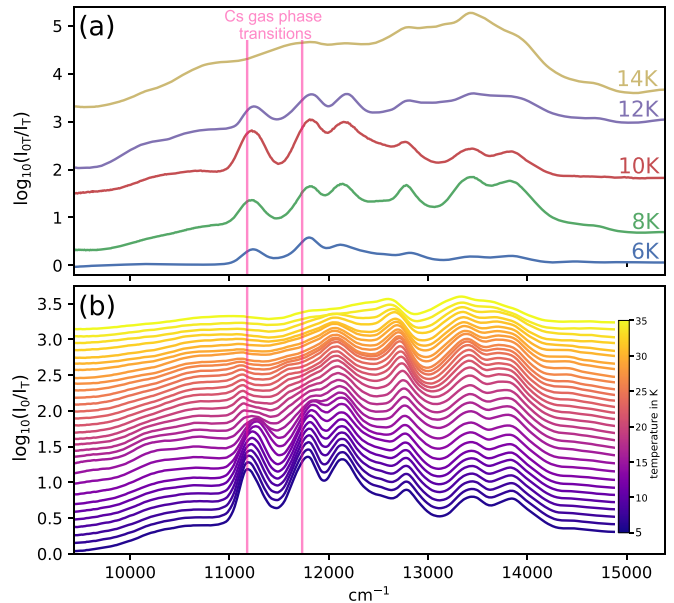


FIG. 2. (a) Absorbance spectra of Cs embedded in Ar deposits conducted at different temperatures. (b) Evolution with temperature for a spectrum initially created at 8 K. The spectra are offset in ordinate for better visual clarity. The positions of the $6s_{1/2} \rightarrow 6p_{1/2}$ (left) and $6s_{1/2} \rightarrow 6p_{3/2}$ (right) Cs gas-phase transitions are indicated for reference.

significantly broader, and we encountered difficulties producing any spectra for deposition temperatures above this.

Conversely, if Cs and Ar are deposited at a low temperature [8 K in the case of Fig. 2(b)], the spectra remain visible even when the sample is subsequently heated up to approximately 35 K, a temperature at which argon begins to sublimate under vacuum.

The spectra show two triplet structures similar to those observed by [17,18], attributed to two types of trapping sites. For comparison, spectra of previous experiments were obtained at 1.8 K in Ref. [18], likely performed at 4.2 K in [17] and performed at 10 K in [19]. Typical positions and widths of the two triplets structures at 8 K are presented in Table I. The differing relative intensities of the two triplets in the various samples [Fig. 2(a)] imply that depending on the deposition conditions (deposit rate, sample density, temperature, argon purity, etc.), one or the other trapping site is favored. It is worth noting that we used slightly different Ar and Cs fluxes

TABLE I. Line center and width extracted from Fig. 2(b) at 8 K. Both triplets were fitted by a sum of three Gaussians.

Line center (cm^{-1})	Line center (nm)	FWHM (cm^{-1})
11 220	891	310
11 780	849	360
12 170	822	350
12 770	783	400
13 400	746	380
13 850	722	400

for different samples. The flux estimates given in the previous section are measured for the sample deposited at 8 K, which will be the one we focus on in the following. For other deposits the rates used can easily vary by a factor of 3.

The temperature evolution shown in Fig. 2(b) shows a more pronounced spectral deformation in the red site (the one between 11 000 and 12 500 cm^{-1}) than in the blue site (the one between 12 500 and 14 000 cm^{-1}). The temperature changes below 20 K are mainly reversible. In the 6–14 K temperature range corresponding to a well-defined red triplet, there is a slight blue shift ($\sim 50 \text{ cm}^{-1}$) of the two lower energy components from 6 K to 14 K, while the position of the highest energy component remains constant. The bandwidths of this triplet structure do not depend on the temperature. Conversely, a slight broadening of the components attributed to the blue site can be inferred from the analysis in Gaussian bands (less than 50 cm^{-1} from 6 to 20 K), while their positions do not shift with temperature. Heating beyond 20 K typically leads to a drop in the baseline (likely due to stronger light scattering in the Ar), along with irreversible changes in the red triplet. The blue site, however, remains well defined until 28 K. Due to the lack of reproducibility, it is not possible to draw more precise conclusions about the evolution of temperature. This information should be handled with care.

More broadly, these types of triplet structures are well documented in alkali-metal atoms trapped in rare gas matrices. They are not due to resolved phonon lines but are created by homogeneous broadening and result from the lifting of the degeneracy of the p level by the crystal environment [4]. However, due to the finite temperature, it is not straightforward to differentiate between the splitting created by a low symmetry crystalline field, as in dislocations or surface defects, and one created by a (temperature-dependent) dynamical Jahn-Teller effect in a more symmetric (cubic, tetrahedral, etc.) crystalline field. From the shape of the lines, however, it already seems evident that the main splitting is on the order of the fine structure splitting between $6p_{1/2}$ and $6p_{3/2}$ (of nearly 554 cm^{-1} in the gas phase). Then the static or dynamical electric crystal field will lift the degeneracy between the $|m| = 3/2$ and $|m| = 1/2$ of the $6p_{3/2}$ level.

B. Trapping sites

1. Potential curves

To explore potential trapping sites within an fcc lattice, we should conduct a stability analysis.

Utilizing a Lennard-Jones potential with an equivalent depth of $\sim 45 \text{ cm}^{-1}$ and an equilibrium distance of $\sim 0.55 \text{ nm}$ as the $X^2\Sigma_{1/2}^+$, Cs-Ar potential [40–42], generic calculations for the accommodation of an atom in fcc and hcp rare-gas solids [6,43] suggest that the likely trapping sites for Cs in an Ar fcc matrix could have six, eight, or potentially ten vacancies with respective symmetries of O_h , C_{2v} , C_{4v} . Nonetheless, a seven-vacancy fcc lattice (C_{3v} symmetry), a five-vacancy trapping site located in an hcp environment, or a grain boundary akin to a stacking fault accommodation (D_{3h} symmetry) could also emerge [5,44].

However, as depicted in Fig. 3(c), the Lennard-Jones potential fails to accurately reproduce the Cs-Ar ground-state

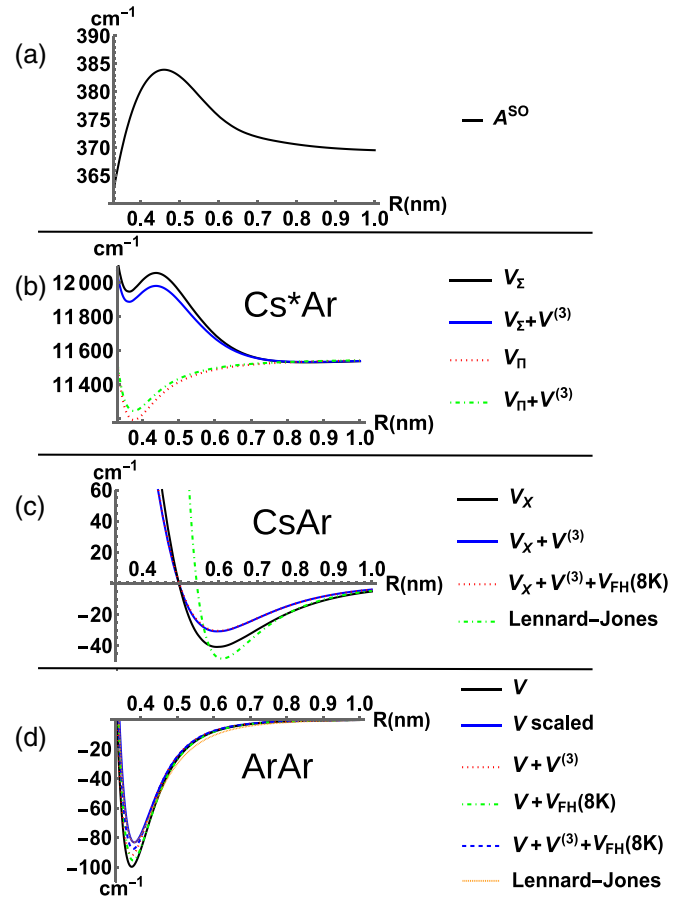


FIG. 3. (a) Spin-orbit constant for Cs($6p$)-Ar interaction. (b) Cs($6p$)-Ar potential curves. (c) Cs($6s$)-Ar potential curves. (d) Ar-Ar ground-state potential curves. The potential curves V used in this study are adjusted by the zero-point energy V_{FH} , and a third-order correction $V^{(3)}$. The original potentials are taken from [41]. For the excited state, we chose to plot only a third-order case with no cutoff (in analogy with the ground-state case; see text), i.e., the two-body potential V [offset by $E(6p)$] multiplied by $\frac{1}{3} \frac{8\pi\rho}{9} \frac{C_6^*}{C_6^0}$.

interaction. Consequently, we conducted our study using more precise potentials.

For the V_{Ar-Ar} potentials, we use the simple analytical formula provided by [45]. For the Cs-Ar ground state $V_{Ar-Cs} = V_{X^2\Sigma_{1/2}^+}$, we employed the potential curve from Ref. [41] with a third-order interpolation between points. Due to a lack of data points in the long-range, we incorporated parts of the potential from [40] for internuclear distances exceeding 2 nm. These potentials are presented in Fig. 3. Although the Lennard-Jones approximation accurately represents the Ar-Ar potential, it is considerably inaccurate for the Cs-Ar potential.

For comprehensive Ar-Ar and Cs-Ar interactions, we use a simple two-body (pairwise potential) approximation. Here the full interaction energy of a Cs-doped crystal with $(N - n)$ Ar atoms and n vacancies is given by the following equation, using obvious notations:

$$V = \sum_{i=1}^{N-n} V_{Ar-Cs}(\mathbf{R}_{Cs-Ar_i}) + \sum_{1 \leq i < j \leq N-n} V_{Ar-Ar}(\mathbf{R}_{ij}). \quad (1)$$

We began by using a simple cubic grid with $N = 4 \times 7^3 = 1372$ atoms (the factor 4 arises from the four atoms in the fcc primitive cell). Convergence is achieved within 1% of the energy for this configuration. This number of atoms enables us to simulate a small homogeneous crystallite that would sit between dislocations.

For a central Ar atom located at \mathbf{R}_0 , the sum over all other atoms $\sum_i V_{\text{Ar-Ar}}(\mathbf{R}_0 - \mathbf{R}_i)$ reaches $\approx 773 \text{ cm}^{-1}$ (here a larger grid is necessary for convergence). This significantly overestimates the experimental value for cohesive energy of 645 cm^{-1} [46,47]. Similarly, the equilibrium distance is established for a lattice constant of 0.521 nm , compared to the correct value of 0.531 nm [47]. To reproduce the correct cohesive (also called atomization $-E_{\text{at}}$) energy and the equilibrium lattice constant, we scaled the Ar-Ar potential by $V = \alpha V_{\text{Ar-Ar}}(\beta R)$ with $\alpha = 645/773$ and $\beta = 0.521/0.531$. Other variants of empirically modified potentials, such as $\alpha V_{\text{Ar-Ar}}(\beta + R)$ used in Ref. [48], yielded similar outcomes. This method is a straightforward way to retain the simple two-body pairwise model while ensuring the appropriate cohesive energy and equilibrium lattice constant. This is achieved by incorporating many-body corrections and zero-point energy effectively [47].

2. Site stability

To evaluate the thermodynamic stability of a structure with n vacancies, we calculate a variant of the Gibbs (or enthalpy) free accommodation energy for the structure [43,49,50]: $\Delta E_N(n) = E_{\text{Cs}}(n, N) - E_{\text{Ar}}(N)(N - n)/N$. Here $E_{\text{Cs}}(n, N)$ signifies the total energy of the system when a Cs atom is introduced into the crystal. Conversely, $E_{\text{Ar}}(N)$ represents the total energy of a pure Ar crystal comprising N atoms, excluding the vacancies.

For the system to exhibit stability, it is crucial that the dissociation of M systems, each containing n vacancies, into M' subsystems with n' vacancies and M'' subsystems with n'' vacancies be energetically unfavorable. This requirement can be represented as $M\Delta E_N(n) < M'\Delta E_N(n') + M''\Delta E_N(n'')$, with the condition $n'M' + n''M'' = nM$ ensuring the conservation of atom numbers. For instance, two systems each with five vacancies can evolve into a more stable configuration of one system with four vacancies and another with six vacancies. Thus, for n vacancies to form a stable trapping site, $\Delta E_N(n)$ must fall within the convex hull of the free energy curve as it varies with the number of vacancies [50,51].

Despite its significance, $\Delta E_N(n)$ is just one of several vital factors, such as migration and activation energies, needed for understanding the trapping sites. The $\Delta E_N(n)$ formula is primarily beneficial for small crystals, or in our case, a small single crystallite in a polycrystal. Alternatively, for $N \rightarrow \infty$, the thermodynamic limit is often applied with $E_{\text{Ar}}(N)/N \approx E_{\text{at}}$, resulting in $\Delta E_N^\infty(n) = E_{\text{Cs}}(n, N) - E_{\text{Ar}}(N) + nE_{\text{at}}$ [52–56].

In order to find the most stable (minimum energy) configuration at a fixed n value, we do not explore the entire position space for the Cs atom and the vacancies through varying random initial configurations. Instead, we initialize with preestablished defect structures in fcc crystals, using positions sourced from existing literature [49,52–62], specifically [63].

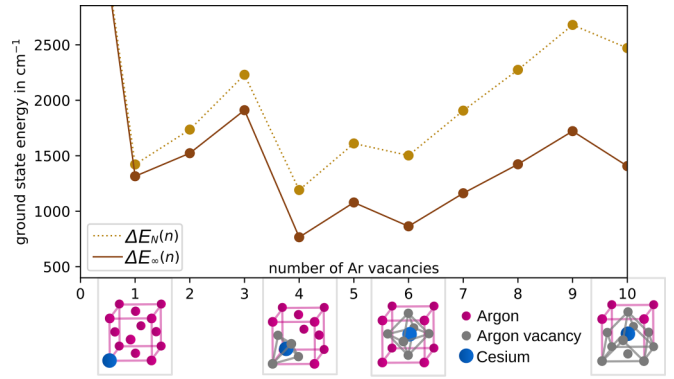


FIG. 4. For a given number of vacancies n , the optimized configuration found to lower $\Delta E(n)$ is displayed (calculation performed with $N = 1372$ atoms). The figure illustrates both $\Delta E(n)$ and $\Delta E^\infty(n)$, alongside a depiction of the final structure realized for the Cs atom and a few of the nearest-neighbor Ar atoms.

In anticipation of the necessity for further studies, such as the Jahn-Teller dynamical effect, we permit the Cs atoms and the initial few layers (typically ~ 60 atoms) of nearest-neighboring Ar atoms to move and optimize their position to minimize $\Delta E_N(n)$ as much as possible. We utilize the Adaptive Moment Estimation (Adam) [64] and its modified version, Nesterov-accelerated Adaptive Moment Estimation (Nadam) [65], collectively considered as “the best overall choice” among gradient descent optimization algorithms [66,67]. Upon nearing the optimum, employing the second-order derivative offers a faster method to adjust the equilibrium position of the normal coordinates [68]. This procedure is iteratively applied, optimizing positions until a minimum is attained. Figure 4 showcases results from such optimized geometries. However, it should be noted that using initial fixed (pure) fcc Ar and vacancy positions suffices to reproduce the results with satisfactory accuracy for stable site predictions, eliminating the need for atomic position optimization.

This study’s findings contrast from the previous one carried out using a Lennard-Jones potential [6,43]. Our study indicates that the most stable trapping sites probably are T_d with four vacancies and O_h with six vacancies. This seems consistent with our observation of two triplet lines in absorption.

C. Simulation of the position of the absorption lines

1. Line positions in the pairwise approach

Contrary to the observations reported by Ref. [19], our data, as shown in Fig. 2, do not show evidence of the Cs($6s \rightarrow 5d$) transition. Only Cs($6s \rightarrow 6p$) triplet structures appear visible, with minimal evidence of any other Cs levels involved. Also Cs dimers seem to be absent at the low density and temperature we are operating at. We are therefore confident that a simple pairwise approximation of the diatomic-in-molecule (DIM) type of approach, involving only the Ar ground state and Cs($6s$), Cs($6p$) levels, should yield accurate results to simulate the Cs($6s \rightarrow 6p$) absorption spectra.

The detailed calculation is outlined in Appendix B. Briefly, the energy shift of the Cs($6s$) is calculated in a similar manner

as was done for the stability study. Now, we include the $6p$ manifold, where the energies are the eigenvalues of the Hamiltonian. These are calculated by summing up the interaction $\langle L'M' | \hat{V}_{\text{Cs,Ar}}(\mathbf{R}_{\text{Cs,Ar}} = \{X, Y, Z\}) | LM \rangle$ between a Cs atom (with $|6pM\rangle$ levels quantized along an arbitrary but fixed axis z) and each Ar atom. This interaction is defined by the matrix obtained using Wigner rotations:

$$\frac{1}{3}[2V_{\Pi}(R) + V_{\Sigma}(R)]\mathbf{I}_3 + \frac{1}{6} \frac{V_{\Sigma}(R) - V_{\Pi}(R)}{R^2} \begin{pmatrix} |M = -1\rangle & |M = 0\rangle & |M = 1\rangle \\ X^2 + Y^2 - 2Z^2 & 3\sqrt{2}(X + iY)Z & -3(X + iY)^2 \\ 3\sqrt{2}(X - iY)Z & -2(X^2 + Y^2 - 2Z^2) & -3\sqrt{2}(X + iY)Z \\ -3(X - iY)^2 & -3\sqrt{2}(X - iY)Z & X^2 + Y^2 - 2Z^2 \end{pmatrix}. \quad (2)$$

Here we also include the spin-orbit $A^{\text{SO}}(R_{\text{Cs,Ar}})\mathbf{L}\cdot\mathbf{S}$ term, where $R = \sqrt{X^2 + Y^2 + Z^2}$.

The Hund's case (a) potential curves $V_{\Pi}(R)$, $V_{\Sigma}(R)$, and the spin-orbit coefficient $A^{\text{SO}}(R)$, where R denotes the Cs-Ar separation, are constructed as shown in Fig. 3. They are based on the most recent $V_{X^2\Sigma_{1/2}^+}$, $V_{A\Pi_{1/2}}$, $V_{A\Pi_{3/2}}$, $V_{B^2\Sigma_{1/2}^+}$ potentials [41]. The long-range part is taken from the potentials of Ref. [40], which provide more points, but are calculated from a smaller basis set and hence are less accurate at short range.

Given that the significant variation of the spin-orbit coefficient $A^{\text{SO}}(R)$ is limited to R values smaller than the distance between the closest neighbours [69], as seen in Fig. 3(a), the use of a constant spin-orbit coefficient A^{SO} yields minimal impact [a maximum shift difference of 10 cm^{-1} in the final Cs($6s$)–Cs($6p$) transition lines]. Hence, in the following analysis, we simply use the V_{Π} , V_{Σ} potential curves and a constant spin-orbit coefficient A^{SO} based on the experimental value.

The big dots in Fig. 5 display the results for the Cs($6s$)–Cs($6p$) transition line positions. In this 0 K theoretical

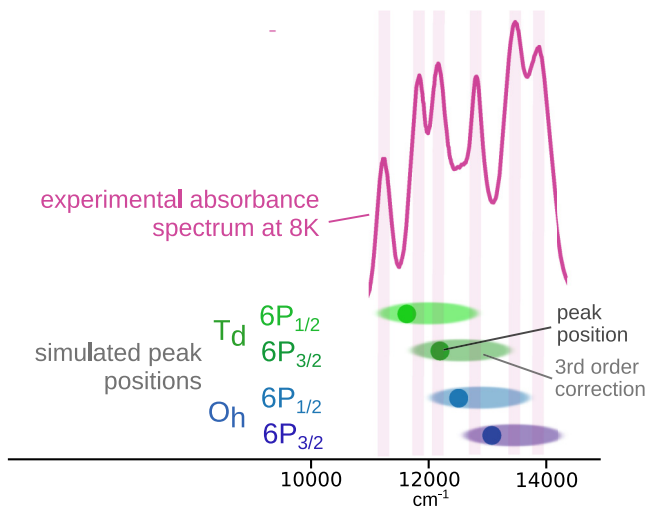


FIG. 5. Comparison between an experimental absorbance spectrum (represented by the solid pink lines), for the two trapping sites, O_h with six vacancies, and T_d with four vacancies. The lower section indicates the position of the 0 K lines employing pairwise potentials, where dots correspond to the two-body cases with potentials sourced from [41]. The influence of zero-point energy on these lines is marginal (at most 150 cm^{-1}). However, the incorporation of the third-order effect (refer to the main text) results in an additional shift that we predict to fall within the elliptical regions.

computation, only doublets emerge, not triplets as would be anticipated in highly symmetric trapping sites, due to the lack of thermal or dynamical broadening. Nevertheless, the experimental and calculated positions show a reasonable degree of agreement.

It may seem surprising initially that the most shifted lines, relative to the gas phase case, are those with six vacancies. This happens while the more constrained structure with four vacancies appears to be hardly affected. The observation that the red triplet is T_d and the blue one is O_h is contrary to what has been noted (or simulated) for other systems such as Na in Ar [70,71]. This discrepancy can be qualitatively explained by a simplified model where Cs is surrounded by Ar atoms in a symmetric spherical environment.

In this spherical context, the average interaction term becomes $2V_{\Pi} + V_{\Sigma}$ [refer to matrix (2)]. Consequently, a valuable approach to study the shift of the $6s$ – $6p$ line position involves examining $2V_{\Pi} + V_{\Sigma} - V_X$. This is demonstrated in Fig. 6, along with the positions of the nearest neighbors in both the T_d and the O_h structures as found in our stability study.

Figure 6 highlights that the blue shift, resulting from positive $\Delta V = 2V_{\Pi} + V_{\Sigma} - V_X$ values, is more pronounced in the O_h case than in the T_d scenario. This difference mainly arises because, in the O_h situation, the first eight and second 24 nearest neighbors (the solvation-type shell) each contributes to a blue shift of approximately 100 cm^{-1} . Meanwhile, in the T_d case, the first shell almost causes no shift due to the

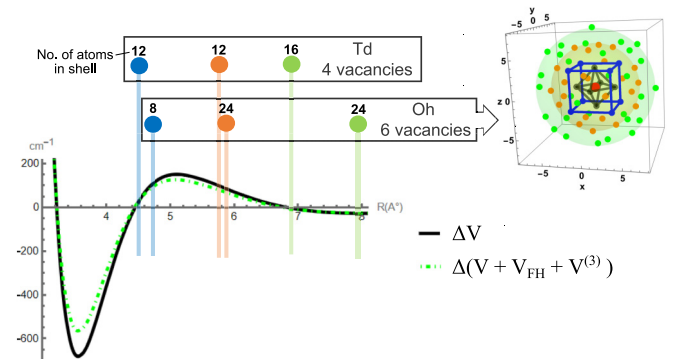


FIG. 6. Illustration of $\Delta V = 2V_{\Pi} + V_{\Sigma} - V_X$ Cs-Ar potentials with an offset of the asymptotic values. The first R_1 , second R_2 , and third R_3 nearest-neighbor shells in the T_d and O_h scenarios are provided (for the O_h case, an example of the Cs and Ar positions is also given).

cancellation of $2V_{\Pi} + V_{\Sigma}$ and V_X shifts, and the second shell contains only 12 atoms. The cumulative effects of these shifts, coupled with the redshifts produced by shells at greater distances, offer a qualitative explanation for the $\sim 2000 \text{ cm}^{-1}$ blue shift in the O_h scenario. Also, the cancellation effect results in T_d lines appearing near the gas phase location.

In line with our approach for Ar-Ar potentials, to enhance the comparison of the line positions, we should include the zero-point energy and third-order many-body interactions. However, as these factors merely provide corrections, we didn't use them to reoptimize the atomic positions.

2. Third-order (dipole-dipole-dipole-type) correction

To the best of our knowledge, the third-order correction has not been previously utilized for simulating absorption spectra [4,71]. However, this correction is non-negligible, particularly for ground states and even more so for excited states.

We currently lack accurate three-body Cs-Ar-Ar potential curves, leading us to approximate their contribution [72,73]. As elaborated in Appendix E, we employ two- and three-body expressions for the pure long dipolar range part to extrapolate an appropriate three-body potential also applicable for shorter distances. Following that, we aggregate it over all atoms. Unfortunately, the nearest neighbors play a significant role [71], and they are in the area where our formula proves to be the least accurate. Consequently, we opt for a simpler approximation, akin to the approach used by Mutô-Stenschke-Marcelli-Wang-Sadus [73–75]. We average the formula, employing a mean-field approach for the position of the third Ar atom, resulting in an effective correction to the two-body Cs-Ar potential.

These are straightforward density-dependent expressions that connect the averaged three-body interactions to the two-body ones. This connection facilitates merging both types of interactions into effective Cs-Ar two-body potential curves. With this methodology, the final Cs-Ar potential curve is a corrected version of the original one, offset by the effective three-body contribution $\bar{E}_{12}^{(3)}$. Ultimately, we obtain an effective two-body potential as described by Eqs. (E9) and (E11).

The influence of this adjustment can be qualitatively estimated from Eq. (E8). By utilizing $2V_{\Pi} + V_{\Sigma} - V_X$ as a measure of the shift, we observe that the third-order effect $\bar{E}_{12}^{(3)}$ displays a $\frac{8\pi\rho}{3R^6}(C_9^* - C_9) > 0$ dependence. This implies a probable net blue shift, where ρ is the Ar density and C_9, C_9^* represent the triple dipole coefficient for the ground and excited states, respectively. This effect can also be interpreted by examining the potential curves provided in Fig. 3. In this figure, the depicted third-order excited state potential curve is computed similarly to the ground-state case. Hence, we have $V_{\Sigma}^{(3)} = [V_{\Sigma} - E(6p)]\frac{1}{3}\frac{8\pi\rho}{9}\frac{C_9^*}{C_9}$ and $V_{\Pi}^{(3)} = [V_{\Pi} - E(6p)]\frac{1}{3}\frac{8\pi\rho}{9}\frac{C_9^*}{C_9}$.

3. Zero-point energy correction

In order to incorporate the quantum effects attributable to the zero-point energy, we utilize the Feynman-Hibbs approach, equivalent to the Wigner-Kirkwood method. This approach introduces a temperature-dependent effective cor-

rection to a pair potential between ground-state atoms, given as $\Delta V_{FH}(R) = \sigma_0^2[V''(R) + 2V'(R)/R]$, where $\sigma_0 = \sqrt{\frac{\hbar^2}{24\mu k_B T}}$ is the Gaussian width of quantum particles, as derived from the uncertainty principle and μ is the reduced mass [76,77].

4. Absorption line positions

Upon integrating the zero-point energy and third-order correction, we find the line positions for the absorption spectra depicted in Fig. 5. In this computation, for the excited states, we applied the effective two-body potential (two-body corrected with three-body), and for the ground state, we additionally incorporated the Feynman-Hibbs zero-point energy correction, $\Delta V_{FH}(R)$, assuming an experimental temperature of 8 K. This procedure was not used for the Ar-Ar interaction, given that we already have a well-scaled potential. However, it is intriguing to validate this method against the known Ar-Ar case. As Fig. 3 suggests, our method of amending a two-body potential with $\Delta V_{FH}(R) + V^{(3)}$ accurately replicates the scaled potential we used.

A key insight is that the zero-point energy is quite negligible (on the order of 100 cm^{-1}), whereas the third-order correction significantly impacts the outcome and thus should not be disregarded. Indeed, the shift generated by the third-order effect is extremely sensitive to the selected cutoff parameters, and it can be either attractive or repulsive, contingent on their values. As such, the induced shift should be viewed more as an indicator of the effect rather than a precise quantitative result, which is why we chose to represent its effect as an uncertainty in our findings. The ellipses in Fig. 5, acting as effective error bars, have been roughly assessed using different cutoff values and exponents in the power of the cutoff function (see Appendix E), along with the potential curves $V_{\Sigma}^{(3)}$ and $V_{\Pi}^{(3)}$ shown in Fig. 3.

Despite the substantial uncertainty of the third order, we can observe a qualitative agreement between theoretical line positions and experimental ones, such as the O_h lines being blue-shifted compared to the T_d ones. However, the correct line separation between O_h and T_d remains elusive. Using theoretical potential curves from Ref. [40] yielded similar results but they were blue-shifted by approximately 1000 cm^{-1} compared to results obtained using the more precise and recent potentials from Ref. [41]). Still, this does not resolve the issue of the line separation between O_h and T_d , which consistently remains around 1000 cm^{-1} , half of the value observed in the experiment. This discrepancy indicates the need for further investigations to reconcile the differences between experimental and simulated positions. High-accuracy Cs-Ar potential curves are required, and better Cs-Ar-Ar third-order calculations, particularly for the nearest-neighbor distances, should be developed.

The line position alone is a good indicator of the trapping site but is not always sufficient to confirm it. Even though the calculated positions for the T_d four-vacancy and O_h six-vacancy cases align with the observation, it is prudent to also consider other stable trapping sites on the convex hull such as the single-vacancy case, where one Ar atom is replaced by a Cs atom, and the 10-vacancy case. The simulation of the absorption lines for the single-vacancy substitution site results

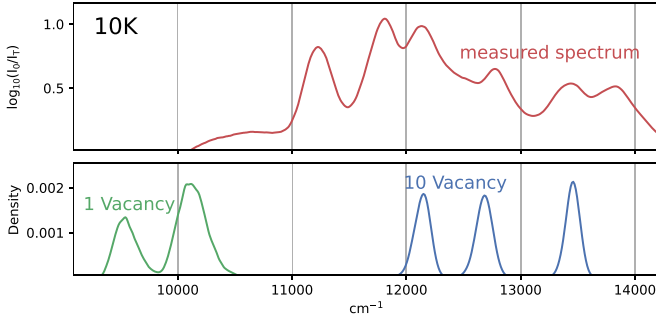


FIG. 7. Comparison between the experimental absorption spectrum and theoretical semiclassical Mulliken formula (4) for the one and 10-vacancy sites at 10 K.

in very red-shifted theoretical lines below 10000 cm^{-1} , where no experimental lines are observed, ruling out this case.

To study the lineshape and not just the central position, we now need to incorporate thermal broadening of the lines due to electron-lattice interaction.

We have already provided the results for the one- and ten-vacancy cases in Fig. 7, confirming that they can likely be dismissed due to the large shift for one vacancy and the overly large and inverted triplet splitting for ten vacancies. Henceforth, we will focus primarily on the four- and six-vacancy cases.

D. Lattice interaction

We must also account for the fact that the nuclei are not stationary, due to zero-point energy and temperature effects.

1. Electron-lattice interaction for nonequilibrium positions

We employ pairwise potentials to compute the electronic ground-state energy $V(\mathbf{R})$ for the positions of the Cs and $(N - n)$ Ar nuclei $\mathbf{R} = \{\mathbf{R}_1, \dots, \mathbf{R}_{N-n+1}\}$ around the equilibrium point (\mathbf{R}_0) , as determined by the stability study.

Subsequently, as detailed in Appendix C, we diagonalize the mass-scaled Hessian matrix, computed via finite difference, to identify the normal mode coordinates \mathbf{Q}^n . The Hessian matrix provides all the oscillation frequencies; this method is a more accurate way of including the zero-point effect than the previously used Feynman-Hibbs formula.

2. Semiclassical approximation for the transitions

To study the laser excitation of the $(6s)$ cesium atom toward the $6p$ manifold under the dipolar operator \hat{d} , we start by noting (using the Beer-Lambert-Bouguer's law) that the spectral density optical absorption coefficient $A(E)$ for a photon of energy E is given by the sum over all initial vibronic levels $|i\rangle$, populated with probability P_i , with state $|\Psi_i\rangle$ of energy E_i , towards all possible final ones $|\Psi_f\rangle$ of energy E_f :

$$A(E) \propto \sum_{f,i} P_i |\langle \Psi_f | \hat{d} | \Psi_i \rangle|^2 \delta[E - (E_f - E_i)]. \quad (3)$$

$A(E)dE$ is the absorption coefficient for a photon in the energy band $(E, E + dE)$. Several approximations are derived in Appendix D. For instance, we neglect the variation of the

dipole $d_{if}(\mathbf{Q})$ with the internuclear distances and assume it to be constant (it is simply the $6s$ to $6p$ dipole transition). We will primarily use two approximations:

$$A(E) \propto \int P_g(\mathbf{Q}) \delta\{E - [V_e(\mathbf{Q}) - V_g(\mathbf{Q})]\} d\mathbf{Q}, \quad (4)$$

$$A(E) \propto \sum_i P_i \int |\Psi_i(\mathbf{Q})|^2 \delta\{E - [V_e(\mathbf{Q}) - E_i]\} d\mathbf{Q}. \quad (5)$$

The first one [Eq. (4)] is called the Mulliken approximation. The second one [Eq. (5)] is referred to as the reflection approximation. $V_e(\mathbf{Q})$ is the excited electron ($6p$) potential energy curve, and $V_g(\mathbf{Q})$ is the ground-state one.

$P_g(\mathbf{Q})$ can be chosen by classical statistics $P_g(\mathbf{Q}) \propto e^{-V_g(\mathbf{Q})/k_B T}$, and the formulas are thus called *classical*. However, it is clearly better to choose the quantum-statistical mechanical probability distribution $P_g(\mathbf{Q}) = \sum_i P_i |\Psi_i(\mathbf{Q})|^2$, in which case we call them *semiclassical*.

Depending on the derivation chosen, the classical Mulliken approximation can be derived from the reflection one with an additional approximation, as in Ref. [78]. Conversely, the reflection approximation can be derived from the Mulliken one, as in Ref. [79]. Hence, it is not clear which formula is the most accurate. However, proper derivation (see Appendix D) tends to favor the (semi)classical Mulliken approximation. Indeed, the Mulliken difference potential $E - [V_e(\mathbf{Q}) - V_g(\mathbf{Q})]$ is known to be a quite good approximation for a Franck-Condon factor [80,81] as it favors transitions where the kinetic energy term is identical between ground and excited state. This is where the phases of the ground and excited wave functions match best, thereby favoring their overlap, as also highlighted by the 1D WKB approximation.

Thus, we start with the semiclassical Mulliken approximation. We will use Monte Carlo integration to estimate the integrals numerically. Due to the spin-orbit interaction and the interaction matrix we have, in the Cs($6p_{1/2}$, $6p_{3/2}$) manifold, six eigenvalues $V_{i,\text{exc}}(\mathbf{Q})$ (the degeneracy of which depends on the symmetry of the trapping sites). The spectra are simply given by summing the histograms of all eigenvalue cases.

3. Phonons thermal effects

At temperature T , the average number of phonons with frequency ω is given by the Bose-Einstein distribution $\bar{n}_\omega = \frac{1}{e^{\hbar\omega/k_B T} - 1}$. The probability of exciting this phonon mode with n quanta [of energy $E_n = (n + 1/2)\hbar\omega$] is given by the geometric distribution $P_n = e^{-n\hbar\omega/k_B T} [1 - e^{-\hbar\omega/k_B T}]$. In the semiclassical approximation, we use the true (quantum) probability distribution function of a harmonic phonon mode of normal mode coordinate Q_ω and angular oscillation frequency ω , as given by [82]: $P_\omega(T) = \frac{1}{\sqrt{2\pi\hbar}[\bar{n}_\omega + 1/2]^{1/2}} e^{-\frac{\omega^2 Q_\omega^2}{2\hbar\omega[\bar{n}_\omega + 1/2]}}$. Thus, if we perform the classical Mulliken calculation with a Boltzmann distribution at a temperature $T' = T'(\omega)$ such that

$$\frac{T'(\omega)}{T} = \frac{\hbar\omega}{k_B T} [\bar{n}_\omega + 1/2] = \frac{\hbar\omega}{2k_B T} \left(\tanh \frac{\hbar\omega}{2k_B T} \right)^{-1}, \quad (6)$$

we will get the correct quantum spectral band contour in the approximation of harmonic motion under the $\frac{1}{2}\omega^2 Q_\omega^2$ potential, as if we had performed the full real quantum calculation

at T . Thus, a classical Mulliken simulation at T' is equivalent to a semiclassical Mulliken simulation at T . This scaled temperature is a way to include phenomenologically the position oscillation due to the zero-point energy in classical simulations [83]. The scaled temperature was used, for instance, to study Na in Ar using molecular dynamic simulation in Ref. [70], where $T = 12$ K and so $T' = 45$ K was used for the pure argon subsystem that thermalizes the Na deposition on other Ar layers.

In argon, the Debye frequency is $\omega_D = k_B \times 93.3 \text{ K}/\hbar$, leading to an effective temperature of $T' \approx 44$ K at low temperatures. Because we have several frequencies (one per mode), we used the scaled temperature $T'(\omega)$ for each of them and chose the mode coordinate Q_ω according to the distribution $P_\omega(T'(\omega)) \propto e^{-\frac{\omega^2 Q_\omega^2}{2k_B T'(\omega)}}$. The energy levels are then calculated for the chosen nucleus position, as done previously for the equilibrium positions. A histogram for the energy difference between excited levels and the ground-state one finally gives the absorption coefficient at each energy according to Eq. (4). For this simulation, only Ar atoms within a specific cutoff distance R_c from the Cs atom are considered. For all simulations presented here, convergence is obtained for $R_c = 3$ nm. This corresponds to approximately 3000 Ar atoms, the positions of which have been optimized to relax the ground-state energy. However, already $R_c = 1$ nm leads to reasonable convergence.

To benchmark our method, we compared it with Na in Ar results from [70] and indeed found very similar absorption spectra for the T_d site.

For our Cs-Ar system, calculations are done with a bare two-body Cs-Ar potential. We found no effect on the shape when adding third-order corrections or when using other potentials such as from [40].

The results for 10 000 samples of the semiclassical Mulliken simulations are given in Fig. 8 for the O_h and T_d cases. However, as discussed previously, the exact position cannot be perfectly reproduced for all presented simulations. Therefore, we shift the theoretical spectra for each O_h and T_d cases. The experimentally observed line broadening is well reproduced, but the triplets are not visible because the splitting of the $6p_{3/2}$ doublet is too low to be resolved. The line positions barely evolve with temperature and the widths only increase by less than 20 cm^{-1} for the considered temperature range. The reason that almost no temperature effect arises is that we have a phonon angular frequencies spectral density very similar to the one for a pure fcc Ar matrix, so ranging from ~ 0 K to the Debye frequency ~ 94 K. Thus, whatever the experimental temperature from $T = 6$ to 14 K, the energy $V_g(\mathbf{Q})$ spanned by the ground-state motion does not vary much with the temperature because the scaled temperature $T'(\omega)$ is always $T'(\omega) \approx \frac{\hbar\omega}{2k_B}$ and that way it is not very sensitive to the actual experimental temperature.

It is interesting to note that a purely classical model using T , not $T'(\omega)$, as done for Na in Ar in Ref. [84], is able to resolve the peak degeneracy and to show temperature effects when T varies. This is an example of a faulty model that gives erroneous results but that might, at first glance, look reasonable.

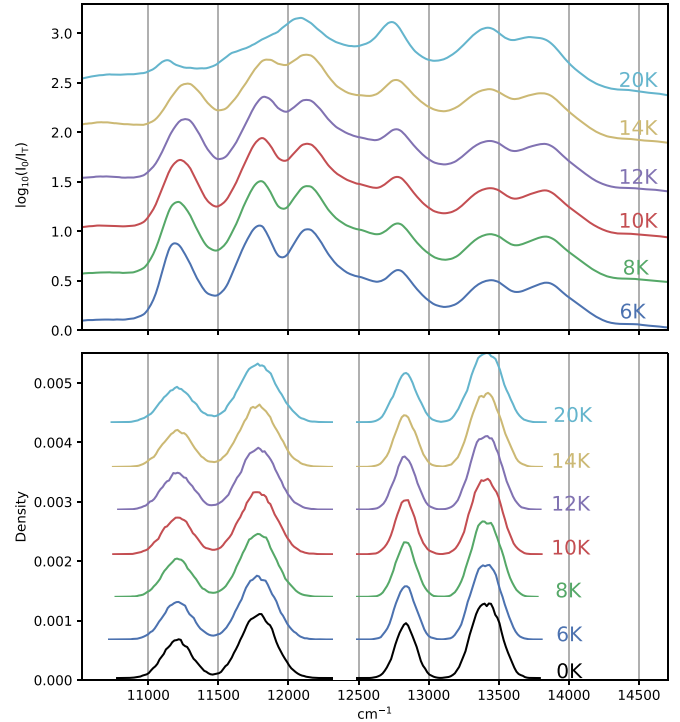


FIG. 8. Comparison between experimental absorption spectra and theoretical semiclassical Mulliken formula [Eq. (4)] at different temperatures $T = 6$ K, 8 K, 10 K, 12 K, 14 K, 20 K and for $T = 0$ K for the theory. The theoretical spectra are created from a kernel density estimation of the Monte Carlo simulation results. The results for the T_d and O_h sites have been shifted in energy by a global offset (which is 500 cm^{-1} and -380 cm^{-1} for O_h and T_d , respectively) to enable easier comparison with the experimental data. For better visual clarity, vertical offsets have been applied to both the experimental and the theoretical spectra.

Another intriguing aspect concerns the fact that a simple crystal field model used in Ref. [18] was able to reproduce the triplet structure quite well. Thus, we now study this crystal field model based only on first-order electron-lattice interaction in order to understand why a simplification of the model might, strangely, give better results than the more complete one we just used.

4. Crystal field: First-order electron-lattice interaction

The crystal-field model is based on the natural expectation that, for better physical insight, it is worth linking the motional modes to the symmetry group of a given trapping site using the so-called crystal-field theory [85].

The normal modes Q^n coordinates have been chosen to obtain a diagonal Hamiltonian with ground-state potential energy given by $\langle 6s|\hat{V}|6s\rangle = V_0 + \sum_k \frac{1}{2}\omega_k^2 Q_k^2$. However, within the Cs($6p$) manifold, these coordinates Q^n are not necessarily the most appropriate anymore. Indeed, if we restrict ourselves to the first-order series in nuclear coordinates, each of the nine coefficients $V_{m',m} = \langle 6pm'|\hat{V}|6pm\rangle$ of the interaction matrix (2), when summed over all Ar positions, contains only linear combinations of the Q^n . Thus, at most nine

different so-called interaction modes matter, each of them being a linear combination of the normal modes. These interaction modes are much more appropriate than the normal modes to give a physical insight into the Cs(6*p*) interaction within the Ar matrix.

They can be calculated when the interactions, so the potential curves, are known. But, in the crystal-field theory, the $Q_{\Gamma\gamma}$ interaction mode coordinates are simply predicted using the symmetries of the trapping site. A given trapping site is an element of a symmetry group with irreducible representations Γ (and its row γ). From it, we find the $Q_{\Gamma\gamma}$, which are the linear combination of the normal modes invariant under the Γ symmetries. The symmetries are also reflected by the electronic wave function that should have an adapted basis set $|\Gamma\gamma\rangle$. Finally, the electron-lattice interaction can be written at first order (so-called crystal-field approximation) as $H_{CF} = V^{(0)}(\mathbf{r}) + \sum_{\Gamma\gamma} V_{\Gamma\gamma}^{(1)}(\mathbf{r})Q_{\Gamma\gamma}$.

Focusing on the 6*p* manifold, the symmetries of the zero-order $V^{(0)}(\mathbf{r})$ potential in the cubic O_h case suggest $\Gamma = T_{1u}$. The adapted electronic basis $|\Gamma\gamma\rangle$ is the 6*p* real (tesseral) spherical harmonics $|x\rangle, |y\rangle, |z\rangle$. Similarly, $\Gamma = T_1$ applies in the T_d case.

To evaluate the first-order term $\sum_{\Gamma\gamma} V_{\Gamma\gamma}^{(1)}(\mathbf{r})Q_{\Gamma\gamma}$ within this basis, we use the Wigner-Eckart theorem [86–88]:

$$\langle \Gamma_1\gamma_1 | V_{\Gamma\gamma}^{(1)} | \Gamma_2\gamma_2 \rangle = \langle \Gamma_1 || \hat{V}_{\Gamma}^{(1)} || \Gamma_2 \rangle \langle \Gamma_1\gamma_1 | \Gamma_2\gamma_2, \Gamma\gamma \rangle. \quad (7)$$

This theorem delivers the selection rules and predicts the nonzero coefficients $\langle \Gamma_1\gamma_1 | V_{\Gamma\gamma}^{(1)} | \Gamma_2\gamma_2 \rangle$ that arise only for some $Q_{\Gamma\gamma}$ [89–91]. The calculations' specifics are presented in Appendix A for multiple symmetry groups in the $|x\rangle, |y\rangle, |z\rangle$ basis. To better align with prior calculations, we also offer the results in the $|m\rangle = |-1, 0, +1\rangle$ basis. Here the Hamiltonian matrix M_{CF} for the T_d case [refer to Eq. (A1)] is given by

$$\begin{pmatrix} V_{A_1}Q_{A_1} - \frac{V_E Q_{E,2}}{\sqrt{3}} & V_{T_2} \frac{iQ_{T_2,1} + Q_{T_2,2}}{\sqrt{2}} & -V_E Q_{E,1} - iV_{T_2} Q_{T_2,3} \\ V_{T_2} \frac{-iQ_{T_2,1} + Q_{T_2,2}}{\sqrt{2}} & V_{A_1}Q_{A_1} + 2\frac{V_E Q_{E,2}}{\sqrt{3}} & V_{T_2} \frac{-iQ_{T_2,1} - Q_{T_2,2}}{\sqrt{2}} \\ -V_E Q_{E,1} + iV_{T_2} Q_{T_2,3} & V_{T_2} \frac{iQ_{T_2,1} - Q_{T_2,2}}{\sqrt{2}} & V_{A_1}Q_{A_1} - \frac{V_E Q_{E,2}}{\sqrt{3}} \end{pmatrix}. \quad (8)$$

For O_h , the results are analogous, with the symmetries' names slightly altered. For simplicity, we maintain these notations for both T_d and O_h in the following discussions. Comparing with the matrix (2) provides physical insight.

The A_1 mode, denoted as Q_{A_1} , which varies as $X^2 + Y^2 + Z^2$, is a radial mode that preserves symmetry. The E_g mode is a tetragonal distortion, represented by $Q_{E,1}$ varying as $X^2 - Y^2$ and $Q_{E,2}$ as $2Z^2 - X^2 - Y^2$. It transforms O_h symmetry into D_{4h} . The T_2 mode bends the crystal to D_{3d} or C_{3v} , with $Q_{T,1}$, $Q_{T,2}$, and $Q_{T,3}$ varying as XZ , YZ , and XY , respectively.

Note that even if the matrix elements are linear in the interaction mode coordinates, the eigenvalues, which are the potential curves, are not linear. Hence, to calculate the Cs(6*s* – 6*p*) absorption spectra, a numerical integration method such as a Monte Carlo simulation is necessary. In the Mulliken formula (4), we have $V_g(\mathbf{Q}) = V_{Cs(6s)-Ar}(\mathbf{Q}) + V_{Ar-Ar}(\mathbf{Q})$ and $V_e(\mathbf{Q}) = V_{Cs(6p)-Ar}(\mathbf{Q}) + V_{Ar-Ar}(\mathbf{Q})$ leading to

$$V_e(\mathbf{Q}) - V_g(\mathbf{Q}) = V_{Cs(6p)-Ar}(\mathbf{Q}) - V_{Cs(6s)-Ar}(\mathbf{Q}). \quad (9)$$

In the linear crystal-field approximation, $V_{Cs(6s)-Ar}(\mathbf{Q})$ is null (or a constant that we offset), hence Eq. (4) simplifies to

$$A(E) \propto \int \sum_{i=1}^6 \delta[E - X_i(\mathbf{Q}^\Gamma)] e^{-\sum_{\Gamma\gamma} \omega_\Gamma^2 Q_{\Gamma\gamma}^2 / 2k_B T} d\mathbf{Q}^\Gamma, \quad (10)$$

where $X_i(\mathbf{Q}^\Gamma)$ are the eigenvalues of M_{CF} plus the spin-orbit matrix (A2), $A^{SO} \mathbf{L} \cdot \mathbf{S}$. This can be estimated using a Monte Carlo method where each $\frac{\omega_\Gamma Q_{\Gamma\gamma}}{\sqrt{k_B T}}$ follows a standard unit normal Gaussian distribution [91].

Assuming in the Boltzmann distribution that the ground-state energy can be written as $V_g(\mathbf{Q}) = \frac{1}{2} \sum_{\Gamma\gamma} \omega_\Gamma^2 Q_{\Gamma\gamma}^2$, which isn't usually the case as $Q_{\Gamma\gamma}$ are not the normal mode coordinates, we found that in our study of the 6*s*–6*p* transition, if projected to the sole “active” coordinates

$Q_{A_1}, Q_{E,1}, Q_{E,2}, Q_{T,1}, Q_{T,2}, Q_{T,3}$, the ground-state Hamiltonian indeed takes the desired quadratic diagonal form.

In this case, as used in Refs. [90,91] (see discussion in Appendix C 3), the oscillation frequencies ω^Γ are not needed for the Mulliken semiclassical case, because we can include them in the definition of scaled coordinates $\tilde{Q}_{\Gamma\gamma} = \frac{\omega_\Gamma}{\sqrt{2}} Q_{\Gamma\gamma}$ with interaction coefficients $\tilde{V}_{\Gamma\gamma} = \frac{\sqrt{2}}{\omega_\Gamma} V$. This leads to $V_{\Gamma\gamma} Q_{\Gamma\gamma} = \tilde{V}_{\Gamma\gamma} \tilde{Q}_{\Gamma\gamma}$, thus Eq. (10) becomes

$$A(E) \propto \int \sum_{i=1}^6 \delta[E - X_i(\tilde{\mathbf{Q}}^\Gamma)] e^{-\sum_{\Gamma\gamma} \tilde{Q}_{\Gamma\gamma}^2 / k_B T} d\tilde{\mathbf{Q}}^\Gamma. \quad (11)$$

Usually, crystal-field theory is used as an effective theory; the parameters $\tilde{V}_{\Gamma\gamma}$ are adjusted to fit the data according to the trapping site symmetry. This fitting process, along with the 6*s* offset for the line position and potential fine structure splitting, typically yields a strong agreement between experiment and theory due to the large number of free parameters.

Compared to the Monte Carlo or molecular dynamics methods, the crystal-field method is significantly faster. It requires only a few parameters (in our case, $\tilde{V}_{A_1}, \tilde{V}_{E,1}, \tilde{V}_{E,2}$) and Gaussian random distributions ($\tilde{Q}_{A_1}, \tilde{Q}_{E,1}, \tilde{Q}_{E,2}, \tilde{Q}_{T,1}, \tilde{Q}_{T,2}, \tilde{Q}_{T,3}$ in our case). Furthermore, the interaction is given by the analytical matrix (8). It is therefore a very attractive method. As previously mentioned in Ref. [18], the observed triplets, similar to our experimental data, were attributed to cubic symmetry sites and were well fitted using the matrix (8) with parameters listed in Table II. The fit was performed at a temperature of $T = 1.8$ K (classically, without any temperature scaling). Using these crystal-field parameters, the calculated line shapes $A(E)$ from Eq. (11) well match the observed shape, and the triplet

TABLE II. Crystal-field parameters, given in degrees Kelvin, for the two types of sites. Oscillation frequencies are such that the ground-state potential is given by $\langle 6s|\hat{V}|6s\rangle = V_0 + \sum_{\Gamma\gamma} \frac{1}{2}\omega_\Gamma^2 Q_{\Gamma\gamma}^2$, while the parameters V_{A_1} , V_E , V_{T_2} serve as coupling parameters for the excited state matrix (8) incorporating linear terms of the $V_\Gamma Q_{\Gamma\gamma}$ type. For comparison, values from the experimental spectrum of Ref. [18] are included.

Site	O_h			T_d		
Mode	A_{1g}	E_g	T_{2g}	A_1	E	T_2
$\hbar\omega_\Gamma/k_B$	60	75	65	64	68	72
$(V_\Gamma/\omega_\Gamma)^2$	50	120	140	110	130	150
$\frac{(V_\Gamma/\omega_\Gamma)^2}{k_B}$ [18]	13 600	84 700	12 600	13 600	84 700	12 600

structure can be resolved. By varying \tilde{V}_{A_1} , \tilde{V}_E , \tilde{V}_{T_2} for the two sites, an almost perfect match can be achieved.

However, the coefficients V_{A_1} , V_E , V_{T_2} can also be computed by comparing the matrix (8) to the gradient of the interaction matrix calculated via the summation of Cs-Ar potentials [refer to Appendix C and formulas (C2) and (C3) for details]. The parameter $(V_\Gamma/\omega_\Gamma)^2$ represents a Jahn-Teller energy shift for the excited potential, evident from the formula $V_\Gamma Q_{\Gamma\gamma} + \frac{1}{2}\omega_\Gamma^2 Q_{\Gamma\gamma}^2 = \frac{1}{2}\omega_\Gamma^2 (Q_{\Gamma\gamma} + \frac{V_\Gamma}{\omega_\Gamma^2})^2 - \frac{1}{2}\frac{V_\Gamma^2}{\omega_\Gamma^2}$. Results are presented in Table II, where frequencies ω_Γ and interaction coefficients V_Γ are displayed in temperature units using $\hbar\omega_\Gamma/k_B$ and $(V_\Gamma/\omega_\Gamma)^2/k_B$.

It is noteworthy that the V_Γ parameters derived from realistic interaction potentials markedly differ from those fitted in Ref. [18]. This shows the risk of using solely crystal-field parameters for fitting, which may not align with physical reality, leading to potential inaccuracies and misleading predictions for subsequent studies [92]. It is therefore crucial to validate them with an independent study, such as magnetic circular dichroism (MCD) [92], temperature dependence of absorption lines, or theoretical predictions [93–96].

Despite these findings, it is important to emphasize that using our derived V_{A_1} , V_E , V_{T_2} coefficients, and limiting our absorption band shape Mulliken semiclassical simulation to the first order in the Q^Γ coordinates for the excited state interaction matrix, we achieve crystal-field results that are nearly identical to those obtained from the full Monte Carlo classical simulation (shown in Fig. 8). Here, excited states are calculated from the full potentials. Indeed, for our temperature range, the first-order matrix element values in the Monte Carlo simulation deviate less than 10% from the actual ones.

In conclusion, both the full potential approach and the crystal-field first-order approximation for the excited state matrix coefficients generate almost identical results. However, they fail to reproduce the observed triplet structure and its temperature evolution. The problem might originate from the inadequacy of the classical model for ground-state motion at low temperatures where the vibrational energies are quantized.

5. Reflection approximation and quantization of the energy

Classical simulations, despite temperature scaling via the appropriate spatial Gaussian distribution $\Psi_i(\mathbf{Q})$, inherently

fall short as they use a continuous energy $P_g(\mathbf{Q})$ in Eq. (4). In contrast, real systems possess quantized ground-state energy E_i . For instance, at low temperatures with only a single zero phonon mode occupation, the ground state exhibits a single energy value, whereas classical simulation permits all energies from 0 to this zero-point energy.

Such a discrepancy suggests that classical simulations can induce artificial line broadening on the order of half the Debye oscillation frequency. In argon, this equates to roughly $\sim 30 \text{ cm}^{-1}$ per vibrational (phonon) mode. While this constitutes an extreme case, given that the majority of lattice vibrations between ground and excited states are similar.

This indicates that the semiclassical Mulliken approximation, often employed to simulate atomic spectra in rare gas matrices may not always be perfectly adequate [44,51,70,71,84,97]. Previous studies have shown that this approximation cannot adequately account for observed line shapes, especially at low temperatures, for the $A \rightarrow T$ spectral band shape ($6s \rightarrow 6p$ is $A_{1g} \rightarrow T_{1u}$ for O_h or $A_1 \rightarrow T_1$ for T_d) [97–99].

In most cryogenic rare gas matrix experiments, a majority of phonon modes exhibit energies significantly larger than the thermal energy, $\hbar\omega \gg k_B T$. As a result, vibronic transitions often occur from zero-phonon occupation, a phenomenon observed in heavy atoms like Eu, Sm, or Yb embedded in Ar [100–104]. Such cases, confined to a single A_1 mode, lead to vibrational quantization that produces well-resolved Huang-Rhys-Pekar-type peaks in the excited states due to the displacement of the harmonic potential in the ground state [105–108]. These peaks can only be elucidated via a full quantum treatment of kinetic energy, as opposed to a semiclassical Franck-Condon-Mulliken approximation.

We are dealing with a particularly complex case: the so-called $T \otimes (a + e + t_2)$ coupling, where a $6p$ triplet T couples with the lattice through several modes plus spin-orbit interaction. This situation bears a strong similarity to the extensively studied Jahn-Teller $T \otimes (e + t_2)$ coupling, which has been investigated using a variety of approximation techniques in full quantum mechanical treatments [94,99,109–111]. Even with some justifiable approximations for our case (see Table II), of a p state equally coupled to E and T vibrations [97], the problem remains intricate. Nevertheless, full quantum treatments seem to agree with classical approaches [91,112].

The optimal path forward to derive a definitive answer would be to perform a full quantum calculation of nuclear motion in the calculation of probability transfers. However, this is outside the scope of this article, as our aim is to use semiclassical expressions to calculate electronic absorption spectra without the need to compute molecular vibrational eigenstates.

In our scenario, most phonon energies $\hbar\omega$ and Jahn-Teller energy shifts $\hbar(V_\Gamma/\omega_\Gamma)^2$ exceed the kinetic energy temperature $k_B T$. Therefore, the reflection approximation in Eq. (5) should provide greater accuracy than the Franck-Condon Mulliken approximation, as it treats the excited-state oscillator classically while the ground state is quantized [78,106].

Regrettably, utilizing the reflection approximation gives rise to numerous complexities. This is particularly true when employing the harmonic approximation, as shown by: $V_g(\mathbf{Q}) = V_{Cs(6s)-Ar}(\mathbf{Q}) + V_{Ar-Ar}(\mathbf{Q}) = \sum_k \frac{1}{2} \omega_k^2 Q_k^2$.

From this, we must calculate the following: $V_e(\mathbf{Q}) - E_i = V_{\text{Cs}(6p)-\text{Ar}}(\mathbf{Q}) - V_{\text{Cs}(6s)-\text{Ar}}(\mathbf{Q}) + \sum_k \frac{1}{2} \omega_k^2 Q_k^2 - E_i$. In this equation, the total quantized ground-state energy $E_i = \sum_k \hbar \omega_k (n_k + 1/2)$ and $\sum_k \frac{1}{2} \omega_k^2 Q_k^2$ both increase linearly with the number of modes. We can bypass this nonphysical divergence by categorizing the modes as either “active” or “passive,” depending on whether they impact $V_{\text{Cs}(6p)-\text{Ar}}(\mathbf{Q}) - V_{\text{Cs}(6s)-\text{Ar}}(\mathbf{Q})$. This can be done using symmetry-adapted coordinates, in which only the six active coordinates significantly affect the Cs interaction with the Ar crystal.

Unfortunately, the ground-state Hamiltonian no longer remains diagonal in the interaction modes, making the energy ill-defined. One possible solution to this problem is to use the fact that, in the low temperature regime, the soft normal coordinates phonon modes with low frequency ($\omega \gtrsim k_B T / \hbar$) are populated. This population results in a different spatial distribution for these normal modes and, thus, for their linear combinations present in the six interaction mode coordinates. For each temperature T , we scale each normal mode frequency, transforming ω into ω' , where $\omega'^2/T = \omega^2/T'(\omega)$, to maintain the correct spatial distribution for the normal modes. The resulting orthonormal transformation produces diagonal $\omega'_{\Gamma\gamma}(T)$ oscillation frequencies for the six interaction mode coordinates. At this temperature T , we simulate a spectrum using the classical Boltzmann distribution, $\propto e^{-\frac{1}{2} \omega'_{\Gamma\gamma}(T)^2 Q_{\Gamma\gamma}^2 / k_B T}$, for each $Q_{\Gamma\gamma}$ and a classical energy $E_i = \sum_{\Gamma\gamma} \frac{1}{2} \omega'_{\Gamma\gamma}(T)^2 Q_{\Gamma\gamma}^2$. The formula used, with \mathbf{Q} representing the interaction mode coordinates, is as follows:

$$A(E) \propto \sum_i P_i \int |\Psi_i(\mathbf{Q})|^2 \delta \left\{ E - \left[V_{\text{Cs}(6p)-\text{Ar}}(\mathbf{Q}) - \sum_k \frac{1}{2} \omega_k'^2 Q_k^2 \right] \right\} d\mathbf{Q}. \quad (12)$$

The results are presented in Fig. 9. This modified reflection approximation restores the triplet shapes, but the splittings do not match closely with the observed ones at the lowest temperature of $T = 6$ K.

Furthermore, the simulated spectra show some temperature-dependent evolution that does not fully align with observed data. Experimentally, the red trapping site (attributed to T_d), and the blue trapping site (attributed to O_h), behave differently with temperature. However, the simulation predicts similar behaviors for O_h or T_d sites, as the Cs(6p) interaction with the Ar matrix is governed by similar couplings (as evidenced by the similar values for the coupling coefficients in Table II). Theoretically we observe, for a Gaussian fit, a redshift of all lines (compare to blueshift of some lines in the experiment) of nearly 30 cm^{-1} for the temperature evolution up to 20 K. We also see a quite strong modification (almost 50%) of the theoretical width, where the experimental evolution is smaller in relative value. Also care must be taken with experimental temperature calibration, as the temperature of a matrix sample may differ from a temperature sensor nearby [113]. There are, however, more critical discrepancies that need to be addressed. The most notable is the mismatch in the splitting between the peaks in the experimental and theoretical data.

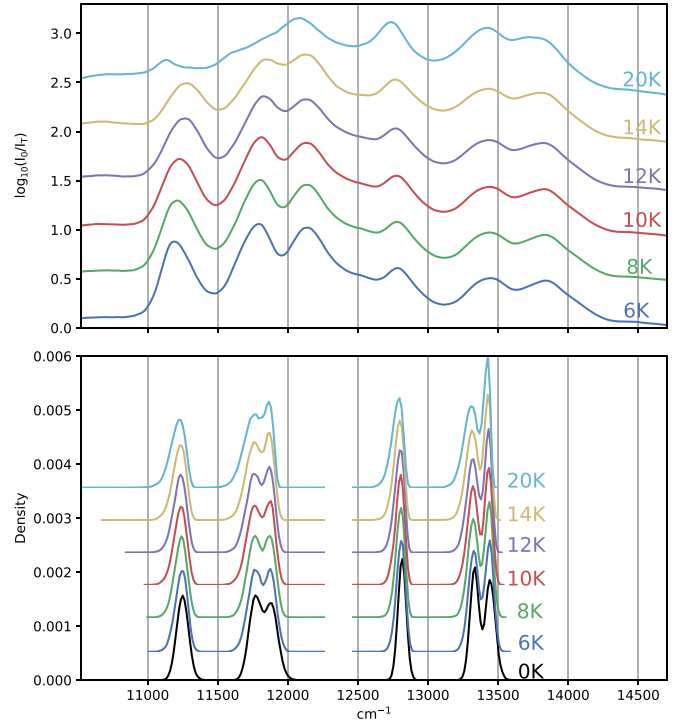


FIG. 9. Comparison of observed absorption with the simulated one using the temperature-scaled first-order crystal-field model. The model incorporates the modified reflection approximation [Eq. (12)], using parameters from Table II. The theoretical spectra are generated from a density kernel estimation of the Monte Carlo simulation results. Results for the T_d and O_h sites are shifted in energy by a global offset for easier comparison with the experimental data (that are 1650 cm^{-1} and 85 cm^{-1} , respectively, for O_h and T_d). Vertical offsets have been applied to both experimental and theoretical spectra to enhance visual clarity.

It remains unclear whether utilizing more sophisticated approximations for the absorption shape would help alleviate these discrepancies. As an example, the improved crystal-field absorption line shape formula proposed in Ref. [98] could be considered. Here S-P transitions are calculated for the most general case, where the coupling of all three vibration modes A_1, E_g, T_2 , as well as spin-orbit interaction, are taken into account. However, because the ω_{Γ} frequencies are almost identical for the T_d and O_h case, this formula may also not produce different temperature evolutions for the two sites.

Further, as highlighted in Ref. [114], semiclassical formulas often require correction when the energy involved is comparable to the quantization energy spacing. However, the proposed corrected terms often have a similar order of magnitude, making the convergence unclear.

Hence, it may be more promising to explore other effects to resolve this discrepancy, such as non-Born-Oppenheimer effects like nonadiabatic coupling.

IV. CONCLUSION

In conclusion, we have observed Cs absorption spectra in an Ar matrix containing six major resonances. These were assigned to transitions from the $6s_{1/2}$ Cs ground state to the

$6p_{1/2}$ and $6p_{3/2}$ excited states, with lifted $|m\rangle$ degeneracy and two different trapping environments. Pairwise Ar-Ar and Cs-Ar potentials facilitated a stability study, indicating that the two observed triplets are likely due to a four-vacancy tetrahedral T_d trapping site and a six-vacancy cubic O_h one in an fcc Ar matrix.

To qualitatively reproduce the line locations using the pairwise approach, we derived effective two-body potential curves. These included zero-point energy and third-order terms. We found that zero-point energy has a minor effect, but adding third-order many-body corrections significantly modifies the potentials. Our derivation of the effective two-body potential from the long-range part of the triple dipolar interaction, based on an exact derivation of the long-range part, is not very accurate. More work is needed on effects such as the Pauli repulsion, exchange interaction, and three-body dispersion interactions for the rare gases: alkali-metal atoms, especially in excited states and for the short-range part [115].

Our study reasonably assigns the nearly unshifted (relative to the gas phase) triplet to the four-vacancy T_d site, and the blue-shifted one to the six-vacancy cubic O_h trapping site. Using the computationally demanding core polarization pseudopotentials will be an interesting approach to confirm this fact and to achieve better agreement between theory and experiment for the line separations [71,116].

Within our current approach, we demonstrate that a triplet shape can be reproduced only by using quantized energy for the ground-state vibrational motions. Indeed, the classical simulation may produce artificial broadening of the lines, on the order of half the Debye oscillation frequency. Therefore, in Ar this would be on the order of $\sim 30 \text{ cm}^{-1}$. Hence, our semiclassical Mulliken simulation fails to produce a triplet structure, instead producing a broad doublet. A simulation using the reflection approximation, on the other hand, yields only a triplet at 0 K, but otherwise diverges with increasing numbers of Ar atoms due to unphysical treatment of the phononic modes.

Finally, a quantized simulation based on a modified reflection approximation reproduces a triplet structure. We show that modifying the population of the soft (low-frequency) phonon modes can also alter the absorption shapes. Using only the matrix gradient (linear, first-order approximation) for the excited state does not alter the quality of the results but leads to significantly faster calculations. Moreover, at low temperatures when only ground-state vibrational (zero-phonon) levels are populated, the simplest crystal-field model suffices to reproduce the observed line broadening caused by the dynamic Jahn-Teller thermal effect. This requires only three electron-lattice parameters given in Table II [together with Eq. (10) and diagonalization of spin-orbit and (8) matrices] [91]. The reduced number of modes is advantageous as it leads to faster calculations than the full Monte Carlo method and captures the essential aspects of the electrostatic interaction, providing a powerful starting point for further studies.

However, our work was unable to reproduce the triplet splitting and did not provide accurate red and blue line separations. The reason for this discrepancy is unclear, but could be due to our neglect of the dipole transition dependence on the Q coordinates, lack of coupling with other excited states

[like Cs($5d$)], or an inappropriate inclusion of the third-order nonadditive terms in the potentials. The role of nonadiabatic couplings should also be studied.

Following [70], modifying the potential curves, such as the $B\Sigma$ state (recently suspected to be inaccurate [117]), might lead to better agreement between experiment and theory. However, our preliminary attempts suggest that substantial modification of the position and the slope of the curve in the region near the first nearest neighbors (see Fig. 6) may be necessary. This should be further investigated, along with experimental and theoretical studies of other possibilities such as trapping in other crystal defects of lower symmetry (for instance, five-vacancy of D_{3h} symmetry in the hcp phase [5,6]), which may explain the discrepancy between experiment and simulation.

Experimentally, many tools are available such as magnetic circular dichroism, fluorescence, electron (paramagnetic) spin resonance, oscillator strength determination, time-resolved emission spectra, nonradiative branching ratios, optical pumping, or bleaching studies. Comparing with the rubidium case and using other rare gases, or even mixed ones, would be interesting [118], to confirm that the matrix shift seen in the S-P transitions is approximately linear with the polarizability of the matrix host [51,70,119].

We hope that our work will be useful for further studies of similar systems used for fundamental physics experiments in rare gas solid crystals [120–122].

ACKNOWLEDGMENTS

T.B. and S.L. contributed equally to this work. This research was financed in whole or in part by Agence Nationale de la Recherche (ANR) under the project ANR-21-CE30-0028-01.

We acknowledge W. Chin, B. Darquier, O. Dulieu, B. Gervais, H. Lignier, Ch. Malbrunot, C. Smai, and B. Viaris for fruitful discussions, and B. Vivan and L. Marriaux for the design and mechanical realization.

APPENDIX A: PERTURBATION MATRICES FOR DIFFERENT SYMMETRIES

A given trapping site is defined by the near neighbor environment of the impurity atom and by its overall crystal orientation in the laboratory frame. We detail here the crystal-field method that we use to simulate the absorption spectrum.

Using vector notation for the cartesian coordinate of each position of the Cs and the $(N - n)$ Ar nuclei $\mathbf{R} = \{\mathbf{R}_1, \dots, \mathbf{R}_{3(N-n+1)}\}$ and \mathbf{r} as the Cs valence electron coordinates, the electron-lattice interaction can be written as $V = V(\mathbf{r}, \mathbf{R})$, where for simplicity, we use in this article the same notation for operators and their representations in coordinate basis.

1. Crystal-field interpretation

A given single trapping site, at the equilibrium position \mathbf{R}_0 , possesses a certain symmetry group with irreducible representation Γ (and its row γ). So it is more convenient to use coordinates, $Q_{\Gamma\gamma}$, that transforms well under such a representation. They are linear combinations of the $R_i - R_{0i}$ ones,

such that at a linear (first-order) approximation, in the nuclear coordinate \mathbf{R} or \mathbf{Q}^Γ , the electron-lattice interaction can be written as $\hat{V} = V^{(0)}(\mathbf{r}) + \sum_{\Gamma\gamma} V_{\Gamma\gamma}^{(1)}(\mathbf{r})\mathcal{Q}_{\Gamma\gamma}$. We refer to this expression as the “crystal-field approximation.”

At zero order, the electron lattice $V^{(0)}(\mathbf{r}) = V(\mathbf{r}, \mathbf{R}_0)$ modifies the Cs electron wave function throughout the $\langle n_1 l_1 m_1 | V^{(0)} | n_2 l_2 m_2 \rangle$ couplings (we use here the nonrelativistic wave functions, without fine structure that depend on the spherical harmonics Y_l^m). The trapping site equilibrium position \mathbf{R}_0 determines the symmetry group for the nuclear environment that produces the electron lattice interaction $V^{(0)}(\mathbf{r})$. For simplicity, we keep the same notation, as for the nuclear coordinate representation Γ , and name the eigenstates of the electronic Hamiltonian that are linear combinations of the $|nlm\rangle$ states, $|\Gamma\gamma\rangle$. They are given by the projection operators for the irreducible representation Γ .

Once the Cs electronic eigenstates $|\Gamma\gamma\rangle$, that are adapted for the ground-state equilibrium position, are found, we can use them to calculate the next order of the electron lattice interaction $\sum_{\Gamma\gamma} V_{\Gamma\gamma}^{(1)}(\mathbf{r})\mathcal{Q}_{\Gamma\gamma}$.

The key result [86,87] is that the $\langle \Gamma_1 \gamma_1 | V_{\Gamma\gamma}^{(1)} | \Gamma_2 \gamma_2 \rangle$ coupling terms can be calculated using the Wigner-Eckart’s theorem $\langle \Gamma_1 \gamma_1 | V_{\Gamma\gamma}^{(1)} | \Gamma_2 \gamma_2 \rangle = \langle \Gamma_1 || \hat{V}_\Gamma^{(1)} || \Gamma_2 \rangle \langle \Gamma_1 \gamma_1 | \Gamma_2 \gamma_2, \Gamma\gamma \rangle$. The nonzero Clebsch-Gordan coefficient $\langle \Gamma_1 \gamma_1 | \Gamma_2 \gamma_2, \Gamma\gamma \rangle$ occurs only if the Γ representation is part of the $\Gamma_1 \times \Gamma_2$ representation [86,87]. Since V is real, we need to consider only the symmetric part of the product: $[\Gamma_1 \times \Gamma_2]$.

Thus, group theory automatically leads to the proper basis $|\Gamma\gamma\rangle$ and provides directly the useful representations Γ with nonzero matrix elements $V_\Gamma = \langle \Gamma_1 || \hat{V}_\Gamma^{(1)} || \Gamma_2 \rangle$ and the Clebsch-Gordan coupling coefficients.

We will now illustrate this crystal-field procedure for several possible trapping site symmetries that might occur for atoms in matrices [49,52–62]. For this we use the free *Mathematica* group theory package GTPack [88,123].

2. Cubic: O_h or T_d symmetry

In fcc crystals, the one-vacancy substitution and the six-vacancy site have both O_h symmetry (same symmetry as the SF_6 molecule) while the four-vacancy site has a T_d symmetry (as CH_4).

For such symmetries, the electron-lattice potential at equilibrium $V^{(0)}(\mathbf{r})$ does not lift the $6s$ nor the $6p$ degeneracy. This

can be understood in a simple manner by decomposing it in spherical harmonics: $V^{(0)}(\mathbf{r}) = \sum_{l,m} r^l a_l^m Y_l^m(\theta, \varphi)$. We now only have to take into account that this interaction potential has necessarily the same O_h or T_d symmetry as the nuclear position that creates it. Thus, most of the terms are zero, and the potential becomes $V^{(0)}(\mathbf{r}) = a_0 Y_0^0 + r^4 a_4 (Y_4^{-4} + \sqrt{14/5} Y_4^0 + Y_4^4) + \dots$ (a_0 is not to be confused with the Bohr radius). These leading order terms formed the so-called Devonshire’s potential [124]. The triangle inequality $|l_1 - l_2| \leq l \leq l_1 + l_2$ for the Clebsch-Gordan coefficients appearing when calculating $\langle n_1 l_1 m_1 | V^{(0)} = \sum_{l,m} r^l a_l^m Y_l^m | n_2 l_2 m_2 \rangle$ indicates that the $l \geq 4$ terms cannot couple to $6s$ ($l = 0$) nor to $6p$ ($l = 1$) states but would lift the degeneracy of the $5d$ ($l = 2$) level, for instance.

For completeness, we indicate that the same calculation can be done elegantly using directly the quantum states $|nlm\rangle$, without using spherical harmonics, by directly writing the potential $\hat{V}(\mathbf{r}, \mathbf{R}_0)$ using angular momentum operators. For this, we simply have to replace, in the Devonshire’s potential expression, $Y_0^0 \rightarrow 1$, $Y_4^{\pm 4} \rightarrow Y_{\pm 4}^4$ and $Y_4^0 \rightarrow 35L_z^4 - (30L(L+1) - 25)L_z^2 + 2L^2(L+1)^2 - 6L(L+1)$ where \mathbf{L} is the orbital angular momentum operator [125,126].

It would be possible to use the $|6sm = 0\rangle$ and $|6pm\rangle = |m\rangle$ basis but for cubic symmetry the so-called real (or tesseral) spherical harmonics: $|x\rangle = (|m = -1\rangle - |m = +1\rangle)/\sqrt{2}$, $|y\rangle = i(|m = -1\rangle + |m = +1\rangle)/\sqrt{2}$, $|z\rangle = |m = 0\rangle$ is better. Indeed, the projection operator technique for the angular momentum basis $|6pm\rangle$ under the symmetry group O_h or T_d and their representations Γ leads to the following: for the $6s$ electronic state $\Gamma = A_{1g}$ (or $\Gamma = A_1$ for T_d) and $|6sm = 0\rangle$ forms a good basis. For the $6p$ electronic states $\Gamma = T_{1u}$ (or $\Gamma = T_1$ in the T_d case) and the basis $|\Gamma\gamma\rangle$ is just given by $|x\rangle$, $|y\rangle$, $|z\rangle$.

Now that the zero-order symmetry $|\Gamma\gamma\rangle$ basis adapted to the nuclear equilibrium configuration is established, we can use it to calculate the first-order correction $\sum_{\Gamma\gamma} \langle \Gamma_1 \gamma_1 | V_{\Gamma\gamma}^{(1)}(\mathbf{r}) | \Gamma_2 \gamma_2 \rangle \mathcal{Q}_{\Gamma\gamma}$. Only the nonzero $\langle 6p = T_{1u} || V^{(1)} || 6p = T_{1u} \rangle$ terms are interesting. Then because $[T_{1u} \times T_{1u}] = A_{1g} \oplus E_g \oplus T_{2g}$ (or $[T_1 \times T_1] = A_1 \oplus E \oplus T_2$ in the T_d case), the $\langle \Gamma_1 \gamma_1 | V_{\Gamma\gamma}^{(1)} | \Gamma_2 \gamma_2 \rangle \mathcal{Q}_{\Gamma\gamma}$ calculation leads to the matrix (with the u, g label removed in the T_d case), in the $6p$ manifold, for the total $\langle \Gamma_1 \gamma_1 | \hat{V} = V^{(0)} + V^{(1)} | \Gamma_2 \gamma_2 \rangle \mathcal{Q}_{\Gamma\gamma}$ crystal-field (CF) interaction:

$$M_{\text{CF}} = \left(\frac{a_0}{\sqrt{4\pi}} + V_{A_{1g}} \mathcal{Q}_{A_{1g}} \right) \mathbf{I}_3 + \begin{pmatrix} |x\rangle & |y\rangle & |z\rangle \\ V_{E_g} (\mathcal{Q}_{E_g,1} - \frac{1}{\sqrt{3}} \mathcal{Q}_{E_g,2}) & V_{T_{2g}} \mathcal{Q}_{T_{2g},3} & V_{T_{2g}} \mathcal{Q}_{T_{2g},2} \\ V_{T_{2g}} \mathcal{Q}_{T_{2g},3} & -V_{E_g} (\mathcal{Q}_{E_g,1} + \frac{1}{\sqrt{3}} \mathcal{Q}_{E_g,2}) & V_{T_{2g}} \mathcal{Q}_{T_{2g},1} \\ V_{T_{2g}} \mathcal{Q}_{T_{2g},2} & V_{T_{2g}} \mathcal{Q}_{T_{2g},1} & V_{E_g} \frac{2}{\sqrt{3}} \mathcal{Q}_{E_g,2} \end{pmatrix}. \quad (\text{A1})$$

Here we have used $V_{A_1} = \langle \Gamma_1 || \hat{V}_{A_1}^{(1)} || \Gamma_2 \rangle / \sqrt{3}$, $V_{E_g} = \langle \Gamma_1 || \hat{V}_{E_g}^{(1)} || \Gamma_2 \rangle / \sqrt{2}$, $V_{T_{2g}} = \langle \Gamma_1 || \hat{V}_{T_{2g}}^{(1)} || \Gamma_2 \rangle / \sqrt{2}$ and performed an orthonormal transformation for the $\{\mathcal{Q}_{E_g,1}, \mathcal{Q}_{E_g,2}\}$ coordinates to obtain the same matrix as the one given in Ref. [91].

This matrix highlights again the fact that, with no thermal effect, so with $\mathcal{Q}_{\Gamma\gamma} = 0$, the $6p$ levels are not lifted by the crystal-field, only a (a_0) global shift of the free transition $6s \rightarrow 6p$ will occur.

In order to complete the calculation, we add the spin degree of freedom with the spin 1/2 basis sets $|\pm\rangle$. The spin-orbit matrix is

$$H_{\text{SO}} = \frac{A^{\text{SO}}}{2} \begin{pmatrix} |x+\rangle & |y+\rangle & |z+\rangle & |x-\rangle & |y-\rangle & |z-\rangle \\ 0 & -i & 0 & 0 & 0 & 1 \\ i & 0 & 0 & 0 & 0 & -i \\ 0 & 0 & 0 & -1 & i & 0 \\ 0 & 0 & -1 & 0 & i & 0 \\ 0 & 0 & -i & -i & 0 & 0 \\ 1 & i & 0 & 0 & 0 & 0 \end{pmatrix}, \quad (\text{A2})$$

and the crystal-field matrix takes a simple block form:

$$H_{\text{CF}} = \begin{pmatrix} M_{\text{CF}} & 0 \\ 0 & M_{\text{CF}} \end{pmatrix}.$$

3. Hexagonal: D_{3h} , C_{3v}

a. Hexagonal: D_{3h}

The D_{3h} symmetry (as C_2H_6 , eclipsed ethane) can arise from five-vacancy in hcp phase, for instance. Its basis vectors are $|E', 1\rangle$, $|E', 2\rangle$, and $|A_2''\rangle = |z\rangle$. The crystal field is, at the lowest order, $V^{(0)}(\mathbf{r}) = a_0^0 Y_0^0 + r^2 a_2 Y_2^0 + \dots$ [with $Y_2^0 = 3L_z^2 - L(L+1)$].

And with $[E' \times E'] = A_1' \oplus E'$ we have

$$M_{\text{CF}} = \left(\frac{a_0}{\sqrt{4\pi}} \right) \mathbf{I}_3 + \begin{pmatrix} |E', 1\rangle & |E', 2\rangle & |z\rangle \\ -\frac{\langle r^2 \rangle a_2}{\sqrt{20\pi}} + V_{E'} Q_{E',1} & V_{A_1'} Q_{A_1'} & 0 \\ V_{A_1'} Q_{A_1'} & -\frac{\langle r^2 \rangle a_2}{\sqrt{20\pi}} + V_{E'} Q_{E',2} & 0 \\ 0 & 0 & \frac{2\langle r^2 \rangle a_2}{\sqrt{20\pi}} \end{pmatrix},$$

where $\langle r^2 \rangle = \langle 6p | r^2 | 6p \rangle$ is the square of the size of a Cs atom in its $6p$ level.

Here the $6p$ ($l=1$) degeneracy is partially lifted into two levels by the crystal field and only the spin orbit will create the triplet structure that is then broadened and modified by the A_1' and E' terms. This symmetry would likely produce a triplet structure.

b. Hexagonal: C_{3v}

The C_{3v} symmetry (as the ammonia NH_3 molecule), can arise from four-vacancy in an hcp phase. It is very similar to the D_{3h} symmetry case and can be obtained from it through the substitutions $E' \rightarrow E$, $A_1' \rightarrow A_1$, and $A_2'' \rightarrow A_1$. Therefore, the basis becomes $|E, 1\rangle$, $|E, 2\rangle$, $|A_1\rangle = |z\rangle$ and the crystal field that at lowest order is given by $V^{(0)}(\mathbf{r}) = a_0^0 Y_0^0 + r^2 a_2 Y_2^0 + \dots$. With $[E \times E] = A_1 \oplus E$ we have

$$M_{\text{CF}} = \left(\frac{a_0}{\sqrt{4\pi}} \right) \mathbf{I}_3 + \begin{pmatrix} |E, 1\rangle & |E, 2\rangle & |z\rangle \\ -\frac{\langle r^2 \rangle a_2}{\sqrt{20\pi}} + V_E Q_{E,1} & V_{A_1} Q_{A_1} & 0 \\ V_{A_1} Q_{A_1} & -\frac{\langle r^2 \rangle a_2}{\sqrt{20\pi}} + V_E Q_{E,2} & 0 \\ 0 & 0 & \frac{2\langle r^2 \rangle a_2}{\sqrt{20\pi}} \end{pmatrix}.$$

This is identical to the previous case, so this symmetry would likely produce a triplet structure.

4. Tetragonal: C_{4v}

The C_{4v} symmetry (as SF_5Cl or IF_5), can arise in the ten-vacancy case. Its basis is $|E, 1\rangle = |x\rangle$, $|E, 2\rangle = |y\rangle$, and $|A_1\rangle = |z\rangle$. The crystal field is at the lowest order: $V^{(0)}(\mathbf{r}) = a_0^0 Y_0^0 + r^2 a_2 Y_2^0 + \dots$, and with $[E \times E] = A_1 \oplus B_2 \oplus B_1$ we get

$$M_{CF} = \left(\frac{a_0}{\sqrt{4\pi}} + V_{A_{1g}} Q_{A_{1g}} \right) \mathbf{I}_3 + \begin{pmatrix} |x\rangle & |y\rangle & |z\rangle \\ -\frac{\langle r^2 \rangle a_2}{\sqrt{20\pi}} - V_{B_2} Q_{B_2} & V_{B_1} Q_{B_1} & 0 \\ V_{B_1} Q_{B_1} & -\frac{\langle r^2 \rangle a_2}{\sqrt{20\pi}} + V_{B_2} Q_{B_2} & 0 \\ 0 & 0 & \frac{2\langle r^2 \rangle a_2}{\sqrt{20\pi}} \end{pmatrix}.$$

This is very similar to the previous cases, and this symmetry would likely produce a triplet structure.

5. Lower symmetry: C_{2v}

The C_{2v} symmetry (as the H_2O water molecule), can arise in the eight-vacancy case and has the basis $|B_2\rangle = |x\rangle$, $|B_1\rangle = |y\rangle$, $|A_1\rangle = |z\rangle$. The crystal field is at the lowest order: $V^{(0)}(\mathbf{r}) = a_0^0 Y_0^0 + r^2 [a_2^0 Y_2^0 + a_2^2 (Y_2^{-2} + Y_2^2)] + \dots$ (with $\hat{Y}_2^{\pm 2} = L_{\pm}^2$) and its matrix takes a diagonal form:

$$M_{CF} = \left(\frac{a_0}{\sqrt{4\pi}} + V_{A_{1g}} Q_{A_{1g}} \right) \mathbf{I}_3 + \frac{\langle r^2 \rangle}{\sqrt{20\pi}} \begin{pmatrix} |x\rangle & |y\rangle & |z\rangle \\ -a_2^0 + \sqrt{6}a_2^2 & 0 & 0 \\ 0 & -a_2^0 - \sqrt{6}a_2^2 & 0 \\ 0 & 0 & 2a_2^0 \end{pmatrix}.$$

Here the $6p$ ($l = 1$) degeneracy is fully lifted in the three levels by the crystal field. The spin-orbit will also shift the levels, and the triplet structure will be broadened in a symmetric way by the A_{1g} terms.

APPENDIX B: POTENTIAL CURVES CALCULATION

We discuss here the Cs-Ar potential for Cs in its $6p$ excited level, the origin of the energy is taken at the $6p$ level in gas phase.

1. Hund's case (a) and (c) curves

Without spin-orbit interaction the Cs($6p$)-Ar interaction is diagonal in the basis $|\Pi, \pm\rangle = |L = 1, M = \pm 1\rangle$, $|\Sigma\rangle = |L = 1, M = 0\rangle$ with $V_{\Pi}(R)$, $V_{\Sigma}(R)$ Hund's case (a) potential curves, where R is the Cs-Ar separation.

When adding the spin-orbit $A^{SO}(R)\mathbf{L}\cdot\mathbf{S}$, the Hamiltonian becomes

$$\begin{pmatrix} |\Pi, +\rangle |m_s = -1/2\rangle & |\Sigma\rangle |m_s = 1/2\rangle & |\Pi, +\rangle |m_s = 1/2\rangle \\ V_{\Pi} - \frac{A^{SO}}{2} & \frac{A^{SO}}{\sqrt{2}} & 0 \\ \frac{A^{SO}}{\sqrt{2}} & V_{\Sigma} & 0 \\ 0 & 0 & V_{\Pi} + \frac{A^{SO}}{2} \end{pmatrix}$$

and the matrix will be identical for the basis with opposite signs for all values of the projection of angular momenta: $|\Pi, -\rangle |m_s = 1/2\rangle$, $|\Sigma\rangle |m_s = -1/2\rangle$, $|\Pi, -\rangle |m_s = -1/2\rangle$. The spin-orbit parameter $A^{SO}(R)$ is not in general constant and deviates from the asymptotic atomic value as shown in Fig. 3 [127]. Taking the eigenvalues leads to the potential curves with spin-orbit $V_{\Pi_{\frac{1}{2}}}$, $V_{\Pi_{\frac{3}{2}}}$, $V_{\Sigma_{\frac{1}{2}}}$ with the correspondence:

$$\begin{aligned} V_{\Sigma} &= \frac{1}{3} (2V_{\Pi_{\frac{1}{2}}} - V_{\Pi_{\frac{3}{2}}} + 2V_{\Sigma_{\frac{1}{2}}} + \sqrt{V_{\Pi_{\frac{1}{2}}}^2 + 2V_{\Pi_{\frac{1}{2}}} V_{\Pi_{\frac{3}{2}}} - 2V_{\Pi_{\frac{3}{2}}}^2 - 4V_{\Pi_{\frac{1}{2}}} V_{\Sigma_{\frac{1}{2}}} + 2V_{\Pi_{\frac{3}{2}}} V_{\Sigma_{\frac{1}{2}}} + V_{\Sigma_{\frac{1}{2}}}^2}), \\ V_{\Pi} &= \frac{1}{6} (V_{\Pi_{\frac{1}{2}}} + 4V_{\Pi_{\frac{3}{2}}} + V_{\Sigma_{\frac{1}{2}}} - \sqrt{V_{\Pi_{\frac{1}{2}}}^2 + 2V_{\Pi_{\frac{1}{2}}} V_{\Pi_{\frac{3}{2}}} - 2V_{\Pi_{\frac{3}{2}}}^2 - 4V_{\Pi_{\frac{1}{2}}} V_{\Sigma_{\frac{1}{2}}} + 2V_{\Pi_{\frac{3}{2}}} V_{\Sigma_{\frac{1}{2}}} + V_{\Sigma_{\frac{1}{2}}}^2}), \\ A^{SO} &= \frac{1}{3} (-V_{\Pi_{\frac{1}{2}}} + 2V_{\Pi_{\frac{3}{2}}} - V_{\Sigma_{\frac{1}{2}}} + \sqrt{V_{\Pi_{\frac{1}{2}}}^2 + 2V_{\Pi_{\frac{1}{2}}} V_{\Pi_{\frac{3}{2}}} - 2V_{\Pi_{\frac{3}{2}}}^2 - 4V_{\Pi_{\frac{1}{2}}} V_{\Sigma_{\frac{1}{2}}} + 2V_{\Pi_{\frac{3}{2}}} V_{\Sigma_{\frac{1}{2}}} + V_{\Sigma_{\frac{1}{2}}}^2}). \end{aligned} \quad (B1)$$

From this correspondence we have extracted the $V_{\Sigma}(R)$ and $V_{\Pi}(R)$ [and $A^{SO}(R)$] potential curves from the $V_{\Pi_{\frac{1}{2}}}$, $V_{\Pi_{\frac{3}{2}}}$, $V_{\Sigma_{\frac{1}{2}}}$ ones. The calculation is done using the most recent $V_{X^2\Sigma_{1/2}^+}$, $V_{A\Pi_{1/2}}$, $V_{A\Pi_{3/2}}$, $V_{B^2\Sigma_{1/2}^+}$ potentials [in Hund's case (a) notation, but calculated with fine structure included] with spin-orbit interactions from [41] and with a cubic interpolation between points and above 2 nm the long-range part is taken from [40].

2. Cs-Ar sum

Using the primitive cell and lattice vectors, we sum the interaction $\langle L'M'|\hat{V}_{Cs,Ar}(\mathbf{R}_{Cs,Ar})|LM\rangle$ between a Cs atom and all Ar ones, where $|LM\rangle = |LM\rangle_z$ is quantized along the fixed z axis.

We then use the fixed right-handed frame, right-hand screw counterclockwise rule active interpretation (extrinsic) rotation $z y z$ convention $\mathcal{R}(\alpha, \beta, \gamma) = e^{-i\alpha L_z} e^{-i\beta L_y} e^{-i\gamma L_z}$ [128,129] such that \mathcal{R} rotates the $|LM\rangle_z$ state to the $|LM\rangle_{\mathcal{R}(z)}$ where the axis $z' = \mathcal{R}(z)$ is along $\mathbf{R}_{Cs,Ar}$. Thus $\mathbf{L}_{\mathcal{R}(z)} = \mathcal{R} \mathbf{L}_z \mathcal{R}^\dagger$. The calculation is done using active rotation of the state vector and Wigner D-matrix with the convention ${}_z \langle LM'|\mathcal{R}(\alpha, \beta, \gamma)|LM\rangle_z = D_{M'M}^L(\alpha, \beta, \gamma) = e^{-i\alpha m' L_z} \langle L'M'|e^{-i\beta L_y}|LM\rangle_z e^{-i\gamma m} = \text{WignerD}[\{L, M', M\}, -\alpha, -\beta, -\gamma]$ (the last notation being adapted for the *Mathematica* software). Using the spherical coordinate, polar angle θ and azimuthal angle φ , for the vector $\mathbf{R}_{Cs,Ar}$ (from Cs to Ar) we have $\alpha = \varphi$, $\beta = \theta$, $\gamma = 0$.

Finally, we find the following matrix for the $\langle L'M'|\hat{V}_{Cs,Ar}(\mathbf{R}_{Cs,Ar})|LM\rangle$ interaction [84,130]:

$$\begin{pmatrix} |\Pi, -\rangle & |\Sigma\rangle & |\Pi, +\rangle \\ \frac{3V_\Pi + V_\Sigma + (V_\Pi - V_\Sigma) \cos(2\theta)}{4} & \frac{e^{i\varphi}(V_\Sigma - V_\Pi) \cos \theta \sin \theta}{\sqrt{2}} & \frac{e^{2i\varphi}(V_\Pi - V_\Sigma) \sin^2 \theta}{2} \\ \frac{e^{-i\varphi}(V_\Sigma - V_\Pi) \cos \theta \sin \theta}{\sqrt{2}} & V_\Sigma \cos^2 \theta + V_\Pi \sin^2 \theta & \frac{e^{i\varphi}(V_\Pi - V_\Sigma) \cos \theta \sin \theta}{\sqrt{2}} \\ \frac{e^{-2i\varphi}(V_\Pi - V_\Sigma) \sin^2 \theta}{2} & \frac{e^{-i\varphi}(V_\Pi - V_\Sigma) \cos \theta \sin \theta}{\sqrt{2}} & \frac{3V_\Pi + V_\Sigma + (V_\Pi - V_\Sigma) \cos(2\theta)}{4} \end{pmatrix} \quad (\text{B2})$$

for a vector \mathbf{R} between the Cs atom and the Ar atoms with X, Y, Z Cartesian coordinate where $\cos(\theta) = Z/R$, $e^{\pm i\varphi} \sin(\theta) = (X \pm iY)/R$. Its Cartesian form is given by Eq. (2).

We then sum over all Ar atoms, using V_Σ and V_Π potentials without spin-orbit interactions in Eq. (2), and after we add a constant spin-orbit interaction that is

$$H_{\text{SO}} = A^{\text{SO}} \begin{pmatrix} |\Pi_- \downarrow\rangle & |\Sigma \downarrow\rangle & |\Pi_+ \downarrow\rangle & |\Pi_- \uparrow\rangle & |\Sigma \uparrow\rangle & |\Pi_+ \uparrow\rangle \\ \frac{1}{2} & 0 & 0 & 0 & 0 & 0 \\ 0 & 0 & 0 & \frac{1}{\sqrt{2}} & 0 & 0 \\ 0 & 0 & -\frac{1}{2} & 0 & \frac{1}{\sqrt{2}} & 0 \\ 0 & \frac{1}{\sqrt{2}} & 0 & -\frac{1}{2} & 0 & 0 \\ 0 & 0 & \frac{1}{\sqrt{2}} & 0 & 0 & 0 \\ 0 & 0 & 0 & 0 & 0 & \frac{1}{2} \end{pmatrix}. \quad (\text{B3})$$

APPENDIX C: VIBRATIONAL MODES

In order to study the vibronic interactions [131] and the Jahn-Teller effect [99,109] we use several different mode coordinates. We will detail here all coordinates we used:

- (i) Cartesian $\mathbf{R} = \{R_j\}$
- (ii) Mass-weighted $\mathbf{Q}^m = \{Q_j^m\} = \mathbf{m}^{1/2}(\mathbf{R} - \mathbf{R}_0)$
- (iii) Normal modes $\mathbf{Q}^n = \{Q_j^n\} = \mathbf{O}_m^\dagger \mathbf{Q}^m$ with oscillations ω_n simply noted ω
- (iv) Interaction modes $\mathbf{Q}^{\text{int}} = \{Q_j^{\text{int}}\} = \mathbf{V}_r^\dagger \mathbf{Q}^n$
- (v) Crystal-field symmetry-adapted interaction modes $\mathbf{Q}^\Gamma = \{Q_{\Gamma\gamma}^\Gamma\} = \mathbf{O}_n^\Gamma \mathbf{Q}^n$ with oscillations ω^Γ
- (vi) Frequency-scaled coordinates $\tilde{\mathbf{Q}}^n = \frac{1}{\sqrt{2}} \omega \mathbf{Q}^n$ or $\tilde{\mathbf{Q}}^\Gamma = \frac{1}{\sqrt{2}} \omega^\Gamma \mathbf{Q}^\Gamma$ with unit oscillations frequencies and their corresponding momenta conjugate, respectively, $\hat{\mathbf{P}}, \hat{\mathbf{P}}_{Q^m}, \hat{\mathbf{P}}_{Q^n}, \hat{\mathbf{P}}_{Q^{\text{int}}}, \hat{\mathbf{P}}_{Q^\Gamma}, \hat{\mathbf{P}}_{\tilde{Q}^n}, \hat{\mathbf{P}}_{\tilde{Q}^\Gamma}$.

1. Quantization in the normal modes

We consider the matrix elements $V(\mathbf{R}) = \langle n'l'm'|\hat{V}|nlm\rangle$ for the Cs(6s) and 6p levels.

Neglecting the anharmonic terms, the electron-lattice crystal field $V = V_0 + \nabla_{\mathbf{R}} V^\dagger (\mathbf{R} - \mathbf{R}_0) + \frac{1}{2} (\mathbf{R} - \mathbf{R}_0)^\dagger \nabla_{\mathbf{R}}^2 V (\mathbf{R} - \mathbf{R}_0)$ is numerically evaluated by finite difference: $\nabla_{\mathbf{R}} V_k = \frac{\partial V}{\partial R_k}(\mathbf{R}^0) \approx \frac{V(\mathbf{R}^0 + \delta R_k) - V(\mathbf{R}^0 - \delta R_k)}{2\delta R_k}$ and $\nabla_{\mathbf{R}}^2 V_{kl} = \frac{\partial^2 V}{\partial R_k \partial R_l}(\mathbf{R}^0) \approx$

$\frac{\frac{\partial V}{\partial R_l}(\mathbf{R}^0 + \delta R_k) - \frac{\partial V}{\partial R_l}(\mathbf{R}^0 - \delta R_k)}{2\delta R_k}$ where we have used standard row vector $\mathbf{R}^\dagger = (R_1, R_2, \dots)$, $\nabla_{\mathbf{R}} V^\dagger = (\frac{\partial V}{\partial R_1}, \frac{\partial V}{\partial R_2}, \dots)$ (\dagger being the Hermitian adjoint, that is, the conjugate transpose) and matrix $\nabla_{\mathbf{R}}^2 V$ notations.

In order to treat all kinetic energy terms $\frac{\hat{p}_k^2}{2m_k}$, ($\hat{p}_k = -i\hbar \frac{\partial}{\partial R_k}$ being the quantized momentum conjugate coordinate) in a similar manner, we use the $3(N - n + 1)$ mass-weighted Cartesian coordinates $Q_j^m = (R_j - R_0) \sqrt{m_j}$ where m_j is the mass of the atom on which the j th coordinate resides. We define the diagonal mass matrix \mathbf{m} with $m_{jj} = m_j$ and $\mathbf{Q}^m \dagger = (Q_1^m, Q_2^m, \dots)$, $\nabla_{\mathbf{Q}^m} \dagger = (\frac{\partial V}{\partial Q_1^m}, \frac{\partial V}{\partial Q_2^m}, \dots)$.

So the nuclear Hamiltonian in the Born-Oppenheimer approximation $\hat{H} = \frac{1}{2} \hat{\mathbf{P}}^\dagger \mathbf{m}^{-1} \hat{\mathbf{P}} + V_0 + \nabla_{\mathbf{R}} V^\dagger (\mathbf{R} - \mathbf{R}_0) + \frac{1}{2} (\mathbf{R} - \mathbf{R}_0)^\dagger \nabla_{\mathbf{R}}^2 V (\mathbf{R} - \mathbf{R}_0)$ becomes simply $\hat{H} = \frac{1}{2} \hat{\mathbf{P}}_{Q^m}^\dagger \hat{\mathbf{P}}_{Q^m} + V_0 + \nabla_{\mathbf{Q}^m} V^\dagger \mathbf{Q}^m + \frac{1}{2} \mathbf{Q}^m \dagger \nabla_{\mathbf{Q}^m}^2 V \mathbf{Q}^m$, where we have used $\hat{\mathbf{P}}_{Q^m} = \mathbf{m}^{-1/2} \hat{\mathbf{P}}$ vector notation for the momentum conjugate with the \mathbf{Q}^m coordinates, that verifies the canonical commutation relation $[\mathbf{Q}^m, \hat{\mathbf{P}}_{Q^m}] = [\mathbf{R}, \hat{\mathbf{P}}] = \mathbf{R} \hat{\mathbf{P}}^\dagger - \hat{\mathbf{P}} \mathbf{R}^\dagger = i\hbar \mathbf{1}$.

The eigendecomposition of the Hessian matrix $\nabla_{\mathbf{Q}^m}^2 V = \mathbf{O}_m^n \omega^2 \mathbf{O}_m^n \dagger$ creates the the normal vibrational modes $\mathbf{Q}^n = \mathbf{O}_m^n \dagger \mathbf{Q}^m$ with \mathbf{O}_m^n the change-of-basis orthonormal matrix and ω a diagonal matrix with the k th element being the

(mass-scaled) oscillation angular frequency ω_k . The Hamiltonian is thus written as

$$\begin{aligned}\hat{H} &= \frac{1}{2}\hat{P}_{Q^n}^\dagger\hat{P}_{Q^n} + V_0 + \nabla_{Q^n}V^\dagger Q^n + \frac{1}{2}Q^{n\dagger}\omega^2Q^n \\ &= \sum_k -\hbar^2\frac{\partial^2}{\partial^2Q_k^n} + V_0 + (\nabla_{Q^n}V^*)_kQ_k^n + \frac{1}{2}\omega_k^2Q_k^{n2}\end{aligned}\quad (\text{C1})$$

with $\nabla_{Q^n}V = \mathbf{O}_m^{n\dagger}\nabla_{Q^m}V$ and $\hat{P}_{Q^n}^\dagger = \mathbf{O}_m^{n\dagger}\hat{P}_{Q^m}$ is the conjugate momentum with $[Q^n, \hat{P}_{Q^n}] = i\hbar\mathbf{1}$.

2. First order: Crystal-field coefficient

We will now use the decomposition (C1) for $V(\mathbf{R}) = \langle 6pm'|\hat{V}|6pm\rangle$.

a. Crystal-field coefficients

In order to determine the (real) crystal-field coefficients V_Γ , that are the $(\nabla_{Q^r}V^\dagger)_{m'm} = \langle m'|\frac{\partial V}{\partial Q_{r\gamma}}|m\rangle$ coefficients present in the 3×3 crystal-field matrix M_{CF} , we restrict ourselves to only the first-order series in nuclear coordinates. Thus, $V = \langle 6pm'|\hat{V}|6pm\rangle$ contains only $(V_0)_{m'm} + (\nabla_{Q^n}V^\dagger)_{m'm}Q^n$ type of terms. We will put the $(\nabla_{Q^n}V^\dagger)_{m'm}$ values in a $3\times 3 = 9$ row matrix, with each row linked to a given m', m .

The first-order potential can be calculated using the normal mode basis Q^n or expressed in the expected M_{CF} crystal-field ones. Equalizing the two expressions leads to the equation $\nabla_{Q^r}V^\dagger Q^\Gamma = \nabla_{Q^n}V^\dagger Q^n$.

Without knowing the orthonormal transformation, $Q^\Gamma = \mathbf{O}_n^{\Gamma\dagger}Q^n$ that links the crystal-field symmetry adapted interaction mode coordinates $Q_{\Gamma\gamma}$ to the normal mode coordinates Q_k^n , the use of the fact that the transformation is orthonormal leads to a 9×9 matrix equation

$$\nabla_{Q^r}V^\dagger\nabla_{Q^r}V = \nabla_{Q^n}V^\dagger\nabla_{Q^n}V \quad (\text{C2})$$

that, when solved, gives the crystal-field coefficients $\nabla_{Q^r}V$.

b. Interaction mode coordinates

In order to perform Monte Carlo simulations, it might be important to know how the crystal-field symmetry adapted interaction mode coordinates Q^Γ can be calculated.

They can be found using the singular value decomposition of the nine-row matrix $\nabla_{Q^n}V^\dagger = \mathbf{U}\mathbf{W}\mathbf{V}^\dagger$ of rank r (the matrix \mathbf{V} not being confused with the potential V). Equation $\nabla_{Q^r}V^\dagger Q^\Gamma = \nabla_{Q^n}V^\dagger Q^n$ leads to $\nabla_{Q^r}V^\dagger Q^\Gamma = (\mathbf{U}\mathbf{W})(\mathbf{V}^\dagger Q^n)$. We cannot simply equalize $\nabla_{Q^r}V^\dagger$ with $\mathbf{U}\mathbf{W}$ and Q^Γ with $\mathbf{V}^\dagger Q^n$ because $Q^{\text{int}} = (\mathbf{V}^\dagger Q^n)$ is only one choice for the interaction mode coordinates, that is not necessarily the same basis (for instance, not in the same order or same sign) as the $Q^\Gamma = \{Q_{\Gamma\gamma}\}$ used to determine from symmetry consideration the crystal-field matrix M_{CF} . However, using the only useful first r rows of the r -block matrix restriction (noted with index r) of $(\mathbf{W}_r)^{-1}\mathbf{U}_r^\dagger(\nabla_{Q^r}V^\dagger \cdot Q^\Gamma) = Q^{\text{int}} = (\mathbf{V}_r^\dagger Q^n)$ leads to the transformation $Q^\Gamma = \mathbf{O}_n^{\Gamma\dagger}Q^n$, where, for simplicity, we have kept the same notation Q^Γ or Q^{int} for the first r interaction modes coordinates than for the $3N$ ones.

The important fact is that the diagonal matrix \mathbf{W} has only r nonzero singular values on the diagonal (so \mathbf{W}_r is square

diagonal of size r), and thus we will often be interested only in the r relevant (r first) interaction mode coordinates.

With these coordinates it turns out that the $r\times r$ matrix $(\omega_\Gamma)^2 = \mathbf{O}_n^{\Gamma\dagger}\omega^2\mathbf{O}_n^\Gamma$ matrix is diagonal. We thus have

$$\langle 6s|\hat{V}|6s\rangle = V_0 + \frac{1}{2}Q^{\Gamma\dagger}(\omega^\Gamma)^2Q^\Gamma = V_0 + \sum_{\Gamma\gamma=1}^r \frac{1}{2}\omega_{\Gamma\gamma}^2Q_{\Gamma\gamma}^2. \quad (\text{C3})$$

Once again, we see the advantage of using the interaction mode coordinates to reduce drastically the number of modes to be calculated. The Monte Carlo simulation becomes very simple because we have to calculate only few ($r \leq 9$) interaction mode coordinates, such as $Q^\Gamma = \{Q_{A_1}, Q_{E,1}, Q_{E,2}, Q_{T,1}, Q_{T,2}, Q_{T,3}\}$ to be compared to $\sim 3N$ modes in standard molecular dynamic simulation (almost 10 000 in our case for the ~ 3000 movable atoms).

3. Frequency-scaled coordinates

Following [90,91], it might be interesting to use the oscillation frequency-scaled coordinates $\tilde{Q}^n = \frac{1}{\sqrt{2}}\omega Q^n$ and $\tilde{Q}^\Gamma = \frac{1}{\sqrt{2}}\omega^\Gamma Q^\Gamma$ such that Eq. (C3) becomes

$$\begin{aligned}\langle 6s|\hat{V}|6s\rangle &= V_0 + \tilde{Q}^{n\dagger}\tilde{Q}^n = V_0 + \sum_k \tilde{Q}_k^{n2} \\ &= V_0 + \sum_{\Gamma\gamma=1}^r \tilde{Q}_{\Gamma\gamma}^2.\end{aligned}$$

This form is interesting, because in a pure classical molecular dynamical simulation, the Boltzmann statistics indicates that \tilde{Q}^n follows a multivariate normal distribution $\propto e^{-\frac{1}{2}\tilde{Q}^{n\dagger}\tilde{\Sigma}^{-1}\tilde{Q}^n}$ with a variance $\tilde{\Sigma}^n = \frac{1}{2}k_B T \mathbf{I}$. That way the interaction mode coordinate vector $\tilde{Q}^\Gamma = \mathbf{O}_n^{\Gamma\dagger}\tilde{Q}^n$ follows a multivariate normal distribution with a variance that is also diagonal: $\tilde{\Sigma}^\Gamma = \mathbf{O}_n^{\Gamma\dagger}\tilde{\Sigma}^n\mathbf{O}_n^\Gamma = \frac{1}{2}k_B T \mathbf{I}$. Thus, in a standard classical Monte Carlo simulation at temperature T , each $\frac{\tilde{Q}_{\Gamma\gamma}}{\sqrt{k_B T/2}}$ coordinate has the same distribution: a standard unit normal (Gaussian).

It is even possible to keep the normalized coordinates in a classical simulation that includes the scaled temperature T' by having \tilde{Q}^n following a multivariate normal distribution with a diagonal variance $\tilde{\Sigma}^{n'}$ with diagonal element given by $\frac{1}{2}k_B T'(\omega_k)$ according to Eq. (6), namely, $\frac{Q_k^n}{\sqrt{k_B T'(\omega_k)/2}}$. In this case, \tilde{Q}^Γ has simply to be chosen with a Gaussian variance $\tilde{\Sigma}^{\Gamma'} = \mathbf{O}_n^{\Gamma\dagger}\tilde{\Sigma}^{n'}\mathbf{O}_n^\Gamma$. Another strategy, that leads to the same final result, is to keep the unit normal distribution for $\frac{Q_k^n}{\sqrt{k_B T/2}}$ but change each ω_k into ω'_k such that $\omega_k^2/T = \omega_k'^2/T'(\omega_k)$.

So, as used in Refs. [90,91], such frequency-scaled coordinates are useful in classical simulations because the oscillation frequencies ω^Γ (or the scaled ones ω'^Γ) of the modes are not needed, if we include them in the definition of crystal-field parameters $\tilde{V}_\Gamma = \sqrt{2}V_\Gamma/\omega_\Gamma$. Then all terms in the interaction matrix can be written using $V_\Gamma Q_{\Gamma\gamma} = \tilde{V}_\Gamma \tilde{Q}_{\Gamma\gamma}$ with now

Eq. (10) becoming Eq. (11) that is

$$A(E) \propto \int \sum_{i=1}^6 \delta[E - X_i(\tilde{\mathbf{Q}}^\Gamma)] e^{-\sum_{\Gamma\gamma} \tilde{Q}_{\Gamma\gamma}^2/k_B T} d\tilde{\mathbf{Q}}^\Gamma \quad (\text{C4})$$

with the $\frac{\tilde{Q}_{\Gamma\gamma}}{\sqrt{k_B T/2}}$ coordinates having a standard unit normal (Gaussian) distribution.

To illustrate this, we mention that the values given in Ref. [18] for the crystal field in Table II are

$$\begin{aligned} A &= \frac{\sqrt{k_B T/2}}{A^{SO}} \tilde{V}_{A_1} = \frac{\sqrt{k_B T/2}}{A^{SO}} \frac{\sqrt{2}}{\omega_{A_1}} V_{A_1} = 0.294, \\ B &= \frac{\sqrt{k_B T/3}}{A^{SO}} \tilde{V}_E = \frac{\sqrt{k_B T/3}}{A^{SO}} \frac{\sqrt{2}}{\omega_E} V_E = 0.6, \\ C &= \frac{\sqrt{k_B T/4}}{A^{SO}} \tilde{V}_{T_2} = \frac{\sqrt{k_B T/4}}{A^{SO}} \frac{\sqrt{2}}{\omega_{T_2}} V_{T_2} = 0.2. \end{aligned}$$

Indeed, the linear part of the potential is $V_{\Gamma\gamma} \mathbf{Q}_{\Gamma\gamma} = A^{SO} \left(\frac{\sqrt{k_B T/x_\Gamma}}{A^{SO}} \frac{\sqrt{2}}{\omega_\Gamma} V_{\Gamma\gamma} \right) \left(\frac{1}{\sqrt{k_B T/x_\Gamma}} \frac{\omega_\Gamma}{\sqrt{2}} \mathbf{Q}_{\Gamma\gamma} \right)$ (x_Γ is 2 for the case of $\Gamma = A_1$, 3 for E_2 and 4 for T_2 [91]). In this notation, the ground-state potential reduces to $\sum_{\Gamma\gamma} \frac{1}{2} \omega_\Gamma^2 \mathbf{Q}_{\Gamma\gamma}^2 = \sum_{\Gamma\gamma} \tilde{Q}_{\Gamma\gamma}^2$.

For the quantized simulation, this frequency-scaled coordinates procedure does not work anymore because the quantized energy levels are intrinsically linked to the frequencies, which thus cannot be simply scaled. We could think of using the frequency-scaled coordinates with unity frequencies such that all modes look similar and the number of different modes would appear to matter less. However this approach is futile because the kinetic energy of the lattice [from Eq. (C1)] would not be diagonal in the momenta conjugate to the scaled interaction mode anymore, as already noticed in Ref. [90]. This is not important in the classical Franck-Condon Mulliken approximation where the kinetic energy plays no role because there, we only need to find the positions that are determined by the Boltzmann distribution involving only the potential energy. It, however, becomes crucial for quantized energies, such as in the reflection approximation.

4. Coordinate distribution

Let us mention that at $T = 0$ K each normal mode $|\Psi_i(\mathbf{Q}_k)|^2$ distribution is gaussian (ground state of the harmonic oscillator) and so the multivariate normal distribution $\propto e^{-\frac{1}{2} \mathbf{Q}^n \Sigma^{-1} \mathbf{Q}^n}$ of the \mathbf{Q}^n normal modes is transformed in a multivariate normal distribution with a variance $\Sigma^\Gamma = \mathbf{O}_n^{\Gamma\dagger} \Sigma^n \mathbf{O}_n^\Gamma$ for the interaction mode. It turns out that the marginal distribution for the six-mode coordinates is indeed a variance that is diagonal. This is a consequence of the fact that the projection on the six-mode coordinates on the ground-state Hessian matrix is diagonal with the frequencies ω^Γ given in Table II. Together with the fact that the first-order approximation is quite accurate for the excited state interaction this leads to the fact that the $T = 0$ K spectra can be calculated in a pure crystal-field model with only six coordinates simply using frequencies ω^Γ to determine the Gaussian \mathbf{Q}^Γ coordinates using temperature scaling or the ground-state wave function of the $\frac{1}{2} \omega_{\Gamma\gamma}^2 \mathbf{Q}_{\Gamma\gamma}^2$ harmonic oscillator. The result for $T = 0$ K gives the same spectra as the one in Fig. 9. Indeed, at $T = 0$ K each E_i is constant and is the zero-point energy of the i th modes. By offsetting to this value, we have at $T = 0$ K, $E_i = 0$ and so the reflection approximation is $A(E) \propto$

$\sum_{i=1}^6 P_i \int |\Psi_i(\mathbf{Q})|^2 \delta\{E - [V_{\text{Cs}(6p)-\text{Ar}}(\mathbf{Q}) - E_i]\} d\mathbf{Q}$ which can be compared to the formula (12).

APPENDIX D: SEMICLASSICAL APPROXIMATIONS

To study laser excitation of the (6s) cesium atom toward the 6p manifold we start (due to the Beer-Lambert-Bouguer's law) by using the fact that the spectral density optical absorption coefficient $A(E)$ for a photon of energy E , is given by the sum over all initial vibronic levels $|i\rangle$, populated with probability P_i with wave function $\Psi_i(\mathbf{Q})$ of energy E_i , towards all possible final ones $\Psi_f(\mathbf{Q})$ of energy E_f :

$$A(E) \propto \sum_{if} P_i \delta[E - (E_f - E_i)] \left| \int \Psi_f^\dagger(\mathbf{Q}) d_{if}(\mathbf{Q}) \Psi_i(\mathbf{Q}) d\mathbf{Q} \right|^2. \quad (\text{D1})$$

Thus $A(E)dE$ is the absorption coefficient for a photon in the energy band $E, E + dE$.

1. Semiclassical Franck-Condon approximation

In our case, the variation of the dipole transition strength from X to Σ or Π states is on the order of 10% [40]. So we can reasonably consider variation of the dipole $d_{if}(\mathbf{Q})$ with the internuclear distances \mathbf{Q} as negligible (this is the ‘‘Condon’’ approximation [78]). If needed, a better approximation would be the Herzberg-Teller centroid one with d_{if} taken at the point $\tilde{\mathbf{Q}}$, which cancels the first-order evolution in \mathbf{Q} . In the following, for simplicity we will assume $d_{if}(\mathbf{Q}) \approx d_{if}(\tilde{\mathbf{Q}})$ to be constant (it is simply the 6s to 6p dipole transition and can thus be left out of the equation). Furthermore, we can also justify an isotropic nature of the dipole in our case because the polycrystalline structure of our sample leads to random orientations of the crystal axes.

In our case, after laser excitation of the Cs(6s) atom from its equilibrium position, the Cs(6p) atom is far from being in its equilibrium position and the excited electron potentials are mostly linear and not quadratic. Thus the motional excited states will be states with large vibrational quantum numbers or even quasicontinuum one, which, according to the Bohr correspondence principle, can be treated as approximately classical. Thus, following [78] we can assume transitions near the classical turning points and for the sum over f we can replace E_f in the δ function by a mean value independent of f that is the electron excited (6p) potential energy curve $V_e(\mathbf{Q})$ so

$$A(E) \propto \sum_i P_i \int \delta\{E - [V_e(\mathbf{Q}) - E_i]\} |\Psi_i(\mathbf{Q})|^2 d\mathbf{Q}. \quad (\text{D2})$$

This expression is also called the reflection approximation [79].

If many initial states (vibrational, for instance) i are involved, it is convenient to use a mean-value approximation using for the ground-state energies, the potential energy $V_g(\mathbf{Q})$ leading to the so-called semiclassical Franck-Condon formula

$$A(E) \propto \int \delta\{E - [V_e(\mathbf{Q}) - V_g(\mathbf{Q})]\} P_g(\mathbf{Q}) d\mathbf{Q} \quad (\text{D3})$$

with $P_g(\mathbf{Q}) = \sum_i P_i |\Psi_i(\mathbf{Q})|^2$ is the quantum-statistical mechanical probability distribution. In the case where $P_g(\mathbf{Q})$ is

given by classical statistics, the expression becomes the standard classical Franck-Condon formula [78].

2. Semiclassical transition in energy or in phase space

It is useful to present the spectral density transition probability $P(E_0)$, for a transition energy E_0 given by Eq. (D1), in a state picture

$$P(E_0) = \sum_{f,i} P_i |\langle \Psi_f | \hat{d} | \Psi_i \rangle|^2 \delta[E_0 - (E_f - E_i)] \quad (\text{D4})$$

because $2\pi P(E_0)/\hbar$ can now be interpreted as a rate given by Fermi's Golden Rule [98,132,133].

This can be written simply (in the Condon or centroid approximation where we forget about d^2 from now on), for a pure state ($P_i = 1$ to simplify the notation) as

$$\begin{aligned} P(E_0) &= \sum_{f,i} \langle \psi_f | \psi_i \rangle \langle \psi_i | \psi_f \rangle \langle \psi_f | \delta[E_0 - (\hat{H}_f - E_i)] | \psi_f \rangle \\ &= \sum_{f,i} \langle \psi_f | \psi_i \rangle \langle \psi_i | \sum_{f'} |\psi_{f'}\rangle \langle \psi_{f'}| \delta[E_0 - (\hat{H}_f - E_i)] | \psi_f \rangle \\ &= \sum_f \langle \psi_f | \left(\sum_i |\psi_i\rangle \langle \psi_i| \delta[E_0 - (\hat{H}_f - E_i)] \right) | \psi_f \rangle \\ &= \text{Tr} \left[\sum_i |\psi_i\rangle \langle \psi_i| \delta[E_0 - (\hat{H}_f - E_i)] \right] \\ &= \text{Tr}[\hat{\rho}_i \delta[E_0 - (\hat{H}_f - E_i)]] \\ &= \langle \delta[E_0 - (\hat{H}_f - E_i)] \rangle \\ &= \langle \delta[E_0 - (\hat{V}_f - \hat{V}_i) - (\hat{H}_f - E_i)] \rangle, \end{aligned}$$

where $\hat{H}_i = \sum_k \hat{p}_k^2/(2m_k) + V_i(\hat{\mathbf{Q}})$ and $\hat{H}_f = \sum_k \hat{p}_k^2/(2m_k) + V_f(\hat{\mathbf{Q}})$ are the Hamilton operators respectively for the initial and final electronic state and $\hat{\rho}_i = \sum_i |\Psi_i\rangle \langle \Psi_i|$ is the density matrix operator for the initial state. The formula can also be written, in the case of a pure state as $P(E_0) = \frac{1}{2\pi\hbar} \int dt e^{i(E_0 - \hat{E}_i)t/\hbar} \langle \Psi_i | \Psi_i(t) \rangle$ where $|\Psi_i(t)\rangle = e^{-i\hat{H}_i t/\hbar} |\Psi_i\rangle$. This time (and Fourier transform) picture opens another way to treat the transition using the (wave packet) time evolution of the system to find $|\psi(t)\rangle$ [114,134–137].

One of the best approximations for the formula is clearly to use $\hat{H}_i - E_i$ as a perturbation, especially when projected on $|\psi_i\rangle$ because $\langle \psi_i | \hat{H}_i - E_i | \psi_i \rangle = 0$. Therefore the simplest natural approximation is the zero-order one for a d -dimensional space:

$$\begin{aligned} P(E_0) &= \langle \delta[E_0 - (\hat{V}_f - \hat{V}_i)] \rangle \\ &= (2\pi\hbar)^{-d} \sum_i \int d\mathbf{Q} |\psi_i(\mathbf{Q})|^2 \delta\{[E - V_f(\mathbf{Q}) + V_i(\mathbf{Q})]\}. \end{aligned} \quad (\text{D5})$$

This is exactly the same as the formula (D3). But note that this derivation differs considerably from the previous traditional derivation despite the final results being the same. For instance, it gives a very clear physical understanding that the reflection approximation of Eq. (5) is reproduced under

the extra approximation of $\delta[E - (H_{f,\text{cl}} - H_{i,\text{cl}})]$ replaced by $\delta\{E - [V_f(\mathbf{Q}) - E_i]\}$.

A very similar derivation has been done by moving to the Wigner representation of quantum mechanics [134,138–142] where the exact formula for $P(E_0)$ becomes, in d dimension, simply $P(E_0) = (2\pi\hbar)^{-d} \int d\mathbf{P} d\mathbf{Q} \rho_{iW} \delta[E_0 - (\hat{H}_f - E_i)]_W$ where $_W$ is designing the Wigner transform. The leading order in \hbar is simply the semiclassical limit with $\hat{H}_{f,i}$ replaced by their classical counterpart $H_{f,i} = \sum_k \hat{p}_k/(2m_k) + V_{f,i}(\mathbf{Q})$ and ρ_{iW} replaced by the classical phase-space density $\rho_{\text{cl}} \propto e^{-H_{\text{cl}}/k_B T}$. It is obviously slightly better to keep the true Wigner function ρ_{iW} (also because it is known analytically for the harmonic potential case) to have [143]: $P(E) = (2\pi\hbar)^{-d} \int d\mathbf{P} d\mathbf{Q} \rho_{iW} \delta[E - (H_{f,\text{cl}} - H_{i,\text{cl}})]$. This is again the same formula (D3) if using the fact that integration of the Wigner function over \mathbf{P} gives exactly the wave function probability distribution $|\psi_i(\mathbf{Q})|^2$ [139]. This derivation has the advantage of justifying the use of the true quantum (or Wigner) phase-space initial distribution and not the classical one. Thus, the probability P_i has to be chosen accordingly to the actual quantum distribution.

Another advantage of this semiclassical phase-space picture is that it allows for systematic series expansion, typically in power of \hbar -order corrections [79,134,136,138,143–146]. Finally, the method can be generalized for nonradiative transitions, such as surface-hopping nonadiabatic effects or electron transfer with instanton theory or other non-Born-Oppenheimer effects [143,147–150].

APPENDIX E: THIRD-ORDER MANY-BODY TERMS

We will detail some calculations to determine the effective two-body potential from the sum of the third-order terms. For this, we will first derive the general expression for the third-order terms and calculate it for the long-range dipolar case and in a simple two-level approximation. This will allow us to create a mean field of long-range third-order terms that we compare to the long-range part of the two-body case. We finally extend this comparison for all internuclear distances to produce an effective two-body potential that includes the third-order effect.

1. Perturbation theory up to third order

The energy shift ΔE of the energy E of the full system of a given atom A (Cs in our case) in a given state $|lm\rangle$ within the crystal formed by many other atoms (Ar in our case) can be estimated by the perturbation theory from the full Hamiltonian energy $H = \sum_i H_0(i) + \frac{1}{2} \sum_{i \neq j} V_{ij}$ where $H_0(i)$ is the single i th atom Hamiltonian and $V_{ij}(\mathbf{r}_i, \mathbf{r}_j, \mathbf{R}_i, \mathbf{R}_j)$ contains all electrostatic interactions between the i th atom and the j th with electron coordinates $\mathbf{r}_i, \mathbf{r}_j$ and nuclear ones $\mathbf{R}_i, \mathbf{R}_j$.

We note the eigenstates of the single-atom Hamiltonian $H_0(i)$ as $|0_i\rangle$ for the initial (not necessarily the ground state in the Cs case) state of atom i of energy E_0 , and $|m_i\rangle$ the other states of energy E_{m_i} .

We calculate the energy shift $\Delta E(\mathbf{R})$ that depends only on the nuclear coordinates \mathbf{R} by perturbation theory. Up to the third order, the full crystal energy is $\frac{1}{2} \sum_{AB} E_{AB}^{(2)} + \frac{1}{6} \sum_{ABC} E_{ABC}^{(3)} = \sum_{A<B} E_{AB}^{(2)} + \sum_{A<B<C} E_{ABC}^{(3)}$. The first order

is zero and the second order leads to a shift depending on atom A given by $\sum_B E_{AB}^{(2)}$ where $E_{12}^{(2)} = \sum_{m_1, m_2} -\frac{|\langle 0_1 0_2 | V_{12} | m_1 m_2 \rangle|^2}{\Delta_{m_1(1)} + \Delta_{m_2(2)}}$ with $\Delta_{m_i}(i) = E_{m_i} - E_0$.

$$E_{123}^{(3)} = \sum_{\sigma \in S_3, m_1, m_2, m_3} \frac{\langle 0_{\sigma(1)} 0_{\sigma(2)} | V_{\sigma(1)\sigma(2)} | m_{\sigma(1)} m_{\sigma(2)} \rangle \langle m_{\sigma(2)} 0_{\sigma(3)} | V_{\sigma(2)\sigma(3)} | 0_{\sigma(2)} m_{\sigma(3)} \rangle \langle m_{\sigma(3)} m_{\sigma(1)} | V_{\sigma(3)\sigma(1)} | 0_{\sigma(3)} 0_{\sigma(1)} \rangle}{[\Delta_{m_{\sigma(1)}}(\sigma(1)) + \Delta_{m_{\sigma(2)}}(\sigma(2))][\Delta_{m_{\sigma(1)}}(\sigma(1)) + \Delta_{m_{\sigma(3)}}(\sigma(3))]} \quad (\text{E1})$$

2. Dipole-dipole-dipole long-range interaction

We will calculate these terms in the dipolar long-range interaction case. We thus assume a dipolar type of interaction (with a fixed quantization axis labeled z). For two atoms labeled 1 and 2 with internuclear separation $\mathbf{R}_{12} = R_{12}\mathbf{e}_{12}$ where \mathbf{e}_{12} is a unit vector, the dipole-dipole interaction is $V_{12} = \frac{e^2}{4\pi\epsilon_0 R_{12}^3} \{ \mathbf{r}(1) \cdot \mathbf{r}(2) - 3[\mathbf{r}(1) \cdot \mathbf{e}_{12}][\mathbf{r}(2) \cdot \mathbf{e}_{12}] \} = \frac{e^2}{4\pi\epsilon_0 R_{12}^3} \mathbf{r}(1) \cdot (1 - 3\mathbf{e}_{12}\mathbf{e}_{12}) \cdot \mathbf{r}(2)$.

That can be written using the irreducible tensors notation, $r_q = r\sqrt{\frac{4\pi}{3}}Y_{1q}(\mathbf{r})$, as $V_{12} = -\frac{e^2}{4\pi\epsilon_0 R_{12}^3} \sqrt{6}C(\mathbf{e}_{12}) \cdot \{ \mathbf{r}(1) \otimes \mathbf{r}(2) \}_2$ where $C_M(\mathbf{e}_{12}) = \sqrt{\frac{4\pi}{5}}Y_{2M}(\mathbf{e}_{12})$ and $\{ \mathbf{r}(1) \otimes \mathbf{r}(2) \}_{2M} = \sum_{q, q'} C_{1q_1 q_2}^{2M} r_{q_1}(1) r_{q_2}(2)$. So

$$V_{12} = -\frac{\sqrt{6}e^2}{4\pi\epsilon_0 R_{12}^3} \sum_{M, q_1, q_2} (-1)^M C_{-M}(\mathbf{e}_{12}) C_{1q_1 q_2}^{2M} r_{q_1}(1) r_{q_2}(2).$$

We will often use atomic units where $\frac{e^2}{4\pi\epsilon_0} = 1$. This can be simply realized by changing $r(i)$ by $r(i)\sqrt{\frac{e^2}{4\pi\epsilon_0}}$.

a. Two-level approximation

One of the simplest approximations is to consider a single effective atomic energy transition, in the pure case, a $S \leftrightarrow P$ transition for each atom [energy difference $E_{SP}(\text{Cs})$ for Cs and $E_{SP}(\text{Ar})$ for Ar]. In our case, all Ar atoms are in the ground state S , but the Cs can be either in ground S or in excited state P . Therefore, S or P degeneracy means that, in Eq. (E1), all energy terms are independent of m_i . We write $\Delta_{m_i}(\sigma(i))$ as $\Delta(\sigma(i))$ that can be factorized out of the sum in Eq. (E1).

Using Cs as atom 1 and Ar for 2 and 3, we have for $i = 2, 3$ $|0_i\rangle = |l=0m=0\rangle$ and $|m_i\rangle = |l=1m=m_i\rangle$ states.

We then follow the elegant derivation done in Ref. [152]. We first look on terms depending on m_2 so for i label for which $\sigma(i) = 2$, in Eq. (E1) we have terms $\langle 0_2 | V(j2) | m_2 \rangle$ and $\langle m_2 | V(2k) | 0_2 \rangle$. So using the Wigner-Eckart theorem $\langle l' m' | r_2^{(q)} | l m \rangle = \frac{C_{lmq}^{l'm'}}{\sqrt{2l'+1}} \langle l' || r_2 || l \rangle$ the $\sum_{m_2} \langle 0_2 | V(j2) | m_2 \rangle \dots \langle m_2 | V(2k) | 0_2 \rangle$ sum (the \dots are simply here to indicate that the terms are not necessarily neighbors in Eq. (E1)) contains $\sum_{m_2} \langle 0_2 | r_{q_2}(2) | m_2 \rangle \dots \langle m_2 | r_{q_2'}(2) | 0_2 \rangle = -\sum_{m_2} C_{1m_2 1q_2}^{00} \dots \frac{C_{00q_2'}^{1m_2}}{\sqrt{3}} \langle 1 || r(2) || 0 \rangle^2$, where we have used $\langle 0 || r(2) || 1 \rangle = -\langle 1 || r(2) || 0 \rangle$. Then $\sum_{m_2=-1}^{m_2=1}$ leads to $\frac{\langle 1 || r(2) || 0 \rangle^2}{3} \delta_{q_2, -q_2'} (-1)^{q_2}$. Similar results arise for atoms 3, for j label for which $\sigma(j) = 3$.

The third-order perturbation theory terms depend on three atoms A, B, and C. Using the symmetry group S_3 of permutations of the three atoms A = 1, B = 2, C = 3, and using $V_{ij} = V_{ji}$, $E_{ABC}^{(3)} = E_{123}^{(3)}$ is the sum of six terms [see [151] (7b)]:

b. Interaction between ground-state atoms

If the Cs atom is in its ground state, the levels are $|0_1\rangle = |l=0m=0\rangle$ and $|m_1\rangle = |l=1m_1\rangle$.

The second order leads to

$$E_{12}^{(2)} = -\frac{C_6}{R_{12}^6}, \quad C_6 = \frac{2}{3} \frac{r_{SP}^2(\text{Cs}) r_{SP}^2(\text{Ar})}{E_{SP}(\text{Cs}) + E_{SP}(\text{Ar})} \quad (\text{E2})$$

with $r_{SP}(\text{Cs}) = \langle 1 || r(1) || 0 \rangle$ and $r_{SP}(\text{Ar}) = \langle 1 || r(2) || 0 \rangle$.

For the third-order calculation, the results we just derived, in Sec. E 2 a, indicate that, in the sum of Eq. (E1), one numerator becomes

$$E = -\frac{\sqrt{6}\sqrt{6}\sqrt{6}}{R_{12}^3 R_{13}^3 R_{23}^3} \frac{\langle 1 || r(1) || 0 \rangle^2}{3} \frac{\langle 1 || r(2) || 0 \rangle^2}{3} \frac{\langle 1 || r(3) || 0 \rangle^2}{3} \times \sum_{q_1, q_2, q_3, q_1', q_2', q_3'} (-1)^{q_1+q_2+q_3} \delta_{q_1, -q_1'} \delta_{q_2, -q_2'} \delta_{q_3, -q_3'} \times \sum_{M, M', M''} (-1)^{M+M'+M''} C_{-M}(\mathbf{e}_{12}) C_{-M'}(\mathbf{e}_{13}) C_{-M''}(\mathbf{e}_{23}) \times C_{1q_1 q_2}^{2M} C_{1q_1' q_2'}^{2M'} C_{1q_2' q_3'}^{2M''},$$

but using (8.4(10) and 8.7(15) from [128]) we have $\sum_{q_1, q_2, q_3} (-1)^{q_1+q_2+q_3} C_{1q_1 q_2}^{2M} C_{1-q_1 q_3}^{2M'} C_{1-q_2 1-q_3}^{2M''} = -(-1)^{-M''} 5C_{2M 2M'}^{2-M''} \begin{Bmatrix} 1 & 1 & 2 \\ 2 & 2 & 1 \end{Bmatrix} = -(-1)^{-M''} C_{2M 2M'}^{2-M''} \sqrt{7/12}$. So

$$E = \frac{\sqrt{14}}{9} \frac{\langle 1 || r(1) || 0 \rangle^2}{R_{12}^3} \frac{\langle 1 || r(2) || 0 \rangle^2}{R_{13}^3} \frac{\langle 1 || r(3) || 0 \rangle^2}{R_{23}^3} \times \sum_{M, M', M''} (-1)^{M+M'} C_{-M}(\mathbf{e}_{12}) C_{-M'}(\mathbf{e}_{13}) C_{-M''}(\mathbf{e}_{23}) C_{2M 2M'}^{2-M''},$$

and finally using the z axis along \mathbf{e}_{12} (so $M = 0$ in the previous sum) and θ_i being the inner angles of the 123 triangle with $\cos \theta_1 = \mathbf{e}_{12} \cdot \mathbf{e}_{13}$ and $\cos(\pi - \theta_2) = \mathbf{e}_{12} \cdot \mathbf{e}_{23}$. We get

$$E = \frac{\langle 1 || r(1) || 0 \rangle^2 \langle 1 || r(2) || 0 \rangle^2 \langle 1 || r(3) || 0 \rangle^2}{36 R_{12}^3 R_{13}^3 R_{23}^3} \times \{ 1 - 3[\cos(2\theta_1) + \cos(2\theta_2) + \cos(2\theta_3)] \}.$$

So when summing the six terms, this finally leads to

$$E_{123}^{(3)} = \frac{4 \langle 1 || r(1) || 0 \rangle^2 \langle 1 || r(2) || 0 \rangle^2 \langle 1 || r(3) || 0 \rangle^2}{36 R_{12}^3 R_{13}^3 R_{23}^3} \times \{ 1 - 3[\cos(2\theta_1) + \cos(2\theta_2) + \cos(2\theta_3)] \} \times \frac{\Delta(1) + \Delta(2) + \Delta(3)}{[\Delta(1) + \Delta(2)][\Delta(2) + \Delta(3)][\Delta(1) + \Delta(3)]}.$$

In summary

$$E_{123}^{(3)} = \frac{C_9}{R_{12}^3 R_{23}^3 R_{31}^3} \frac{1 - 3[\cos(2\theta_1) + \cos(2\theta_2) + \cos(2\theta_3)]}{4},$$

$$C_9 = \frac{4}{9} r_{SP}^2(\text{Cs}) r_{SP}^4(\text{Ar}) \frac{E_{SP}(\text{Cs}) + 2E_{SP}(\text{Ar})}{2[E_{SP}(\text{Cs}) + E_{SP}(\text{Ar})]^2 E_{SP}(\text{Ar})}. \quad (\text{E3})$$

We wrote the C_9 coefficient such that we can restore the historical Axilrod-Tenner-Mutô [153,154] form using $1 - 3[\cos(2\theta_1) + \cos(2\theta_2) + \cos(2\theta_3)] = 4[1 + 3\cos(\theta_1)\cos(\theta_2)\cos(\theta_3)]$.

These calculations are technical but similar in a way to the case of two atoms under the effect of a static external electric field [155], the physical picture of the dipole of one atom (1, for instance) interacting with the vector electric fields produced by the other dipoles (2) and (3) helps to understand that the final result depends on the angles and distance between atoms.

c. Interaction with Cs in an excited state $|l = 1m\rangle$

To our knowledge, no general simple formula has been derived for the dipole-dipole-dipole interaction with one atom in the excited state (see, however, Ref. [156] and references therein). We derive one formula here. For this, we start with the fact that in this case, $|0_1\rangle = |l = 1m\rangle$ and $|m_1\rangle = |l = 0m = 0\rangle$. So

$$\begin{aligned} & \sum_{m_1} \langle 0_1 | r_{q_1}(1) | m_1 \rangle \dots \langle m_1 | r_{q'_1}(1) | 0_1 \rangle \\ &= \langle 1m | r_{q_1}(1) | 00 \rangle \dots \langle 00 | r_{q'_1}(1) | 1m \rangle \\ &= -C_{1m1q'_1}^{00} \frac{C_{001q_1}^{1m}}{\sqrt{3}} \langle 1 || r(1) || 0 \rangle^2 \\ &= \delta_{mq_1} \delta_{q_1, -q'_1} (-1)^{q_1} \frac{\langle 1 || r(1) || 0 \rangle^2}{3}. \end{aligned}$$

The second order leads to $C_6^* = \frac{2}{3} \frac{\langle 1 || r(1) || 0 \rangle^2 \langle 1 || r(2) || 0 \rangle^2}{\Delta(1) + \Delta(2)}$ with

$$E_{12}^{(2)} = -\frac{2C_6^*}{3R_{12}^6} = -\frac{C_6^*(\Sigma)}{R_{12}^6} \text{ for } m = 0,$$

$$E_{12}^{(2)} = -\frac{C_6^*}{6R_{12}^6} = -\frac{C_6^*(\Pi)}{R_{12}^6} \text{ for } m = \pm 1,$$

$$C_6^* = \frac{2}{3} \frac{r_{SP}^2(\text{Cs}) r_{SP}^2(\text{Ar})}{E_{SP}(\text{Ar}) - E_{SP}(\text{Cs})}, \quad (\text{E4})$$

so as expected $C_6^*(\Sigma) + 2C_6^*(\Pi) = C_6^*$.

For the third order, we have for a given numerator term:

$$E = -\frac{\sqrt{6}\sqrt{6}\sqrt{6}}{R_{12}^3 R_{13}^3 R_{23}^3} \frac{\langle 1 || r(1) || 0 \rangle^2}{3} \frac{\langle 1 || r(2) || 0 \rangle^2}{3} \frac{\langle 1 || r(3) || 0 \rangle^2}{3}$$

$$\times \sum_{q_1, q_2, q'_1, q'_2, q_3, q'_3} \delta_{mq_1} \delta_{q_1, -q'_1} (-1)^{q_1+q_2+q_3} \delta_{q_2, -q'_2} \delta_{q_3, -q'_3}$$

$$\times \sum_{M, M', M''} (-1)^{M+M'+M''} C_{-M}(\mathbf{e}_{12}) C_{-M'}(\mathbf{e}_{13}) C_{-M''}(\mathbf{e}_{23})$$

$$\times C_{1q_1 1q_2}^{2M} C_{1q'_1 1q_3}^{2M'} C_{1q'_2 1q'_3}^{2M''},$$

but using z axis along \mathbf{e}_{12} (so $M = 0$) we have

$$E = -\sqrt{\frac{8}{27}} \frac{\langle 1 || r(1) || 0 \rangle^2}{R_{12}^3} \frac{\langle 1 || r(2) || 0 \rangle^2}{R_{13}^3} \frac{\langle 1 || r(3) || 0 \rangle^2}{R_{23}^3}$$

$$\times \sum_{M', M''} (-1)^{M'+M''} C_0(\mathbf{e}_{12}) C_{-M'}(\mathbf{e}_{13}) C_{-M''}(\mathbf{e}_{23})$$

$$\times C_{1m1-m}^{20} \sum_{q_3} (-1)^{q_3} C_{1-m1q_3}^{2M'} C_{1m1-q_3}^{2M''}.$$

So $E = \frac{\langle 1 || r(1) || 0 \rangle^2 \langle 1 || r(2) || 0 \rangle^2 \langle 1 || r(3) || 0 \rangle^2}{54 R_{12}^3 R_{13}^3 R_{23}^3} f(\theta_1, \theta_2, \theta_3, m)$ with

$$f(\theta_1, \theta_2, \theta_3, m) = -[1 + 3\cos(2\theta_1) + 3\cos(2\theta_2) + 9\cos(2\theta_3)] \text{ for } m = 0, \quad (\text{E5})$$

$$f(\theta_1, \theta_2, \theta_3, m) = [5 - 3\cos(2\theta_1) - 3\cos(2\theta_2) + 9\cos(2\theta_3)]/4 \text{ for } m = \pm 1. \quad (\text{E6})$$

Then summing the six terms (see [152]) finally leads to

$$E_{123}^{(3)} = \frac{2\langle 1 || r(1) || 0 \rangle^2 \langle 1 || r(2) || 0 \rangle^2 \langle 1 || r(3) || 0 \rangle^2}{27 R_{12}^3 R_{13}^3 R_{23}^3}$$

$$\times f(\theta_1, \theta_2, \theta_3, m)$$

$$\times \frac{\Delta(1) + \Delta(2) + \Delta(3)}{[\Delta(1) + \Delta(2)][\Delta(2) + \Delta(3)][\Delta(1) + \Delta(3)]},$$

so

$$E_{123}^{(3)} = \frac{C_9^*}{R_{12}^3 R_{13}^3 R_{23}^3} \frac{f(\theta_1, \theta_2, \theta_3, m)}{6},$$

$$C_9^* = \frac{4}{9} r_{SP}^2(\text{Cs}) r_{SP}^4(\text{Ar}) \frac{2E_{SP}(\text{Ar}) - E_{SP}(\text{Cs})}{2[E_{SP}(\text{Ar}) - E_{SP}(\text{Cs})]^2 E_{SP}(\text{Ar})}. \quad (\text{E7})$$

3. Mean-field effect and effective two-body potentials

The most accurate way to include this third-order correction for the energy of atoms A is to sum over all B and C pairs of atoms. But due to the lack of information on the short-range part and due to the crude (two-level) estimation made up to now, we can simplify the problem further and use the mean-field approach done in Ref. [74] (see also [73,157]) by creating a mean-field potential $\bar{E}_{AB}^{(3)} = \sum_C E_{ABC}^{(3)}$ such that the full crystal energy $\frac{1}{2}(\sum_{AB} E_{AB}^{(2)} + \frac{1}{3} \sum_{ABC} E_{ABC}^{(3)})$ can be written as sum of two-body terms $E_{AB}^{\text{eff}} = E_{AB}^{(2)} + \frac{1}{3} \bar{E}_{AB}^{(3)}$.

We can thus stay at a two-body level simply by modifying the two-body interaction between atoms by adding $\frac{1}{3} \bar{E}_{AB}^{(3)}$ to the $E_{AB}^{(2)}$ potential interaction curves we already have. This mean-field approach has been proven to be quite accurate for pure crystals, as shown by the so-called Marcelli-Wang-Sadus potential [73,77,157–160] and as we demonstrate in Fig. 3 in the Ar-Ar case.

a. Mean-field homogeneous assumption

Strangely enough, almost no mathematical derivation of the mean-field approach exists though it has been performed as back as in the original paper by Mutô [154] (whose journal reference is almost always wrong) and by Stenschke [74]. Following these works, we replace the sum $\bar{E}_{AB}^{(3)} =$

$\sum_C E_{ABC}^{(3)}$ by an integral assuming Ar atoms uniformly distributed with density $\rho = N/V$ (for solid argon the density $\rho = a_0^{-3}/280$ where a_0 is the Bohr radius). We thus sum over the C atoms (number 3 above); that is, we average the potential $V = \sum_j E_{12j}^{(3)}$ as $\bar{V} = \rho \int V r^2 \sin \theta dr d\theta d\varphi = 2\pi \rho \int V r^2 \sin \theta dr d\theta$ in spherical coordinate with $\theta = \theta_1$ and $r = R = R_{12}$. We found simpler to use $r_1 = R_{13}$, $r_2 = R_{23}$ coordinates, as in Ref. [74], such that $\bar{V} = 2\pi \rho \int V \frac{r_1 r_2}{R} dr_1 dr_2$, with an exclusion sphere of radius σ around the atoms A = 1 and B = 2. Equations (E3) and (E7) lead to

$$\begin{aligned} \bar{E}_{12}^{(3)} &= 2\pi \rho \frac{C_9}{R^6} \frac{4}{3}, \\ E_{12}^{*(3)} &= 2\pi \rho \frac{C_9^*}{R^6} \frac{4}{9} \{4 - 3 \log[(R^2 - \sigma^2)/\sigma^2]\} \text{ for } m = 0, \\ E_{12}^{\pm(3)} &= 2\pi \rho \frac{C_9^*}{R^6} \frac{2}{9} \{-1 + 3 \log[(R^2 - \sigma^2)/\sigma^2]\} \text{ for } m = \pm 1. \end{aligned} \quad (\text{E8})$$

Therefore, the triple dipole interaction does not depend on σ only when the state is isotropic, such as the S ground state, or when summing over $m = -1, 0, 1$ for the P state.

b. Effective potentials

All results are summarized by Eqs (E2)–(E8) from where we can extract the effective potentials for the internuclear distance R :

$$\begin{aligned} E_{AB}^{\text{eff}}(R) &= E_{AB}^{(2)}(R) \left(1 - \frac{8\pi \rho C_9}{9 C_6}\right), \\ E_{AB}^{*,\text{eff}}(\Sigma) &= E_{AB}^{(2)}(\Sigma) \left\{1 - \frac{4\pi \rho C_9^*}{9 C_6^*} \left[4 - 3 \log\left(\frac{R^2 - \sigma^2}{\sigma^2}\right)\right]\right\}, \\ E_{AB}^{\pm,\text{eff}}(\Pi) &= E_{AB}^{(2)}(\Pi) \left\{1 - \frac{8\pi \rho C_9^*}{9 C_6^*} \left[-1 + 3 \log\left(\frac{R^2 - \sigma^2}{\sigma^2}\right)\right]\right\}. \end{aligned} \quad (\text{E9})$$

This form, derived from the long-range triple dipole interaction, can however naturally be extended to the full range of the potential by simply keeping the same formula for all R . The only requirement is the choice of the cutoff because $R > 2\sigma$. Because the short-range part of the potential is clearly not a dipole-dipole one, we smoothly reduce the C_9^* part for $R < 2\sigma$ by multiplying it in Eq. (E9), for all R , by a sharp cutoff function $1 - e^{-(R/2\sigma)^{10}}$. A reasonable value for σ might be the nearest-neighbor distance in the fcc crystal, the lattice size or the first nearest-neighbor Cs-Ar atoms in a given trapping site (see Fig. 6). This may depend on the chosen trapping site to be studied. Another cutoff, in principle independent, should be of the order of the LeRoy radius that corresponds to the change in the multipole expansion at small R . In that case the theoretical curves are too different from the long-range part, which we used to derive the formula [161,162]. From all this, we found that a reasonable value can be $\sigma \sim 8 a_0$. However, all these parameters (cutoffs and the power 10 in the sharp function) are arbitrary choices that can be optimized. We have modified them a bit (typically by a factor of 2) to produce the uncertainty in the line position shown in Fig. 5.

c. Approximate calculation of C_6 and C_9 coefficients

Our previous formulas for second-order perturbations Eqs. (E2) and (E4), and third-order perturbations Eqs. (E3) and (E7), contain the van der Waals interaction coefficients C_6, C_6^*, C_9, C_9^* , which we now need to evaluate. For this, we will use an effective two-level approximation, known to be 25% accurate for ground-state interactions between rare-gas and alkali-metal atoms [72,163], and that we are going to use for the excited states as well. We will also compare the value found by fitting them to the long-range part of our potential curves to existing results to assess the method accuracy. From now on, we will use atomic units for this calculation.

The atomic unit value for the C_6 coefficient for Ar-Ar, found by fitting the theoretical Ar-Ar potential curve by $-C_6/R^6$, is 67; and 380 for Ar-Cs. Using Eq. (E2) with the well-known experimental values, $E_{SP}(\text{Cs}) \approx 0.0524$ and $E_{SP}(\text{Ar}) \approx 0.43$ for the first excited P levels, leads to $r_{SP}(\text{Cs}) = 5.4$ and $r_{SP}(\text{Ar}) = 3.0$.

These values are acceptable because they are reasonable: the C_6 Cs-Cs coefficient is 5500 (compare to the real value of nearly 6700 [164]); $C_9(\text{Ar-Ar-Ar}) \approx 650$ (compared to 525 in Refs. [163,165]); and $C_9(\text{Cs-Cs-Cs}) \approx 1\,500\,000$ (compared to $C_9(\text{Cs-Cs-Cs}) \approx 2\,200\,000$ in Ref. [72]). However, these values for $r_{SP}(\text{Cs})$, $r_{SP}(\text{Ar})$, $E_{SP}(\text{Cs})$, and $E_{SP}(\text{Ar})$ lead to quite wrong values for the excited Cs*-Ar coefficient of $C_6^*(\Sigma) = \frac{2}{3}C_6^* = 310$ compared to 600 in our potential curves and $C_6^*(\Pi) = \frac{1}{6}C_6^* = 80$ compared to 270. Unfortunately, it is not possible to solve this discrepancy for all excited states at once simply because Eq. (E4) gives a ratio 4 between $C_6^*(\Sigma)$ and $C_6^*(\Pi)$ while in our case, the theoretical potential curves give only a factor ~ 2 . This factor 2 is indeed found in many other cases [166,167].

This discrepancy probably comes from the fact that we have neglected other excited states [like Cs(7s)] that are quite near the Cs excited (6p) level. But, because our intention is to simulate the Cs spectrum in argon, we will focus more on the Cs-Ar and Cs*-Ar interaction curves than on the Ar-Ar one in order to try to reduce the discrepancy. For this, we choose an intermediate strategy and allow modification of the dipole transitions $r_{SP}(\text{Cs})$, $r_{SP}(\text{Ar})$ and the energy level $E_{SP}(\text{Ar})$, that become effective values. This allows us to better reproduce the long-range part of the theoretical potential curve for Cs-Ar and Cs*-Ar. For this, we start with fitting the theoretical potential curve that leads to $\frac{C_6^*}{C_6} \approx 3$. Then Eqs. (E2) and (E4) give $\frac{C_6^*}{C_6} = \frac{E_{SP}(\text{Ar}) + E_{SP}(\text{Cs})}{E_{SP}(\text{Ar}) - E_{SP}(\text{Cs})}$. This leads to

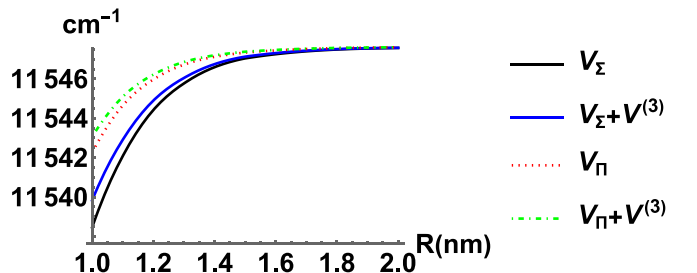


FIG. 10. Cs(6p)-Ar potential curves compared to the one with the effective third-order effect included.

$E_{SP}(\text{Ar}) = 2E_{SP}(\text{Cs}) = 0.10$. Then, using expression Eq. (E2) for the C_6 coefficient for Ar-Ar (67) and Ar-Cs (380) leads to (in atomic units)

$$E_{SP}(\text{Cs}) = 0.052, \quad (\text{E10})$$

$$E_{SP}(\text{Ar}) \approx 0.10,$$

$$r_{SP}(\text{Cs}) \approx 4.4,$$

$$r_{SP}(\text{Ar}) \approx 2.1,$$

$$C_6 \approx 370,$$

$$C_6^* \approx 1200,$$

$$C_9 \approx 9100,$$

$$C_9^* \approx 54\,000. \quad (\text{E11})$$

The long-range parts of some potential curves are shown in Fig. 10. These parameter values, and the modification by a factor ~ 2 for the cutoff and the power of the sharp function, have been used in order to produce the uncertainty in the line positions shown in Fig. 5.

-
- [1] A. Barnes, W. Orville-Thomas, A. Müller, and R. Gaufrès, *Matrix Isolation Spectroscopy* (Springer, Dordrecht, 1981).
- [2] M. Almond and A. Downs, *Spectroscopy of Matrix Isolated Species* (Wiley, Chichester, 1989).
- [3] V. E. Bondybey, A. M. Smith, and J. Agreiter, *Chem. Rev.* **96**, 2113 (1996).
- [4] C. Crepin-Gilbert and A. Tramer, *Int. Rev. Phys. Chem.* **18**, 485 (1999).
- [5] B. M. Davis, B. Gervais, and J. G. McCaffrey, *J. Chem. Phys.* **148**, 124308 (2018).
- [6] G. K. Ozerov, D. S. Bezrukov, and A. A. Buchachenko, *Phys. Rev. B* **103**, 184110 (2021).
- [7] C. Pryor and F. Wilczek, *Phys. Lett. B* **194**, 137 (1987).
- [8] M. Arndt, S. Kanorsky, A. Weis, and T. Hänsch, *Phys. Lett. A* **174**, 298 (1993).
- [9] M. G. Kozlov and A. Derevianko, *Phys. Rev. Lett.* **97**, 063001 (2006).
- [10] A. C. Vutha, M. Horbatsch, and E. A. Hessels, *Atoms* **6**, 3 (2018).
- [11] S. Upadhyay, U. Dargyte, V. D. Dergachev, R. P. Prater, S. A. Varganov, T. V. Tscherebul, D. Patterson, and J. D. Weinstein, *Phys. Rev. A* **100**, 063419 (2019).
- [12] C. Braggio, R. Calabrese, G. Carugno, G. Fiscelli, M. Guarise, A. Khanbekyan, A. Noto, R. Passante, L. Rizzuto, G. Ruoso, and L. Tomassetti, *Appl. Sci.* **12**, 6492 (2022).
- [13] D. Budker, T. Cecil, T. E. Chupp, A. A. Geraci, D. F. Jackson Kimball, S. Kolkowitz, S. Rajendran, J. T. Singh, and A. O. Sushkov, [arXiv:2203.09488](https://arxiv.org/abs/2203.09488).
- [14] M. S. Safronova, D. Budker, D. DeMille, D. F. J. Kimball, A. Derevianko, and C. W. Clark, *Rev. Mod. Phys.* **90**, 025008 (2018).
- [15] C. Ien, V. Bowers, E. Cochran, and S. Foner, *Phys. Rev.* **126**, 1749 (1962).
- [16] J. Goldsborough and T. Koehler, *Phys. Rev.* **133**, A135 (1964).
- [17] W. Weyhmann and F. Pipkin, *Phys. Rev.* **137**, A490 (1965).
- [18] T. Kanda and T. Ebisu, *J. Phys. Soc. Jpn.* **31**, 957 (1971).
- [19] L. Balling and J. Wright, *J. Chem. Phys.* **78**, 592 (1983).
- [20] J. L. Hollenberg and D. A. Dows, *J. Chem. Phys.* **37**, 1300 (1962).
- [21] P. Groner, I. Stolkin, and H. H. Gunthard, *J. Phys. E: Sci. Instrum.* **6**, 122 (1973).
- [22] G. J. Jiang, W. B. Person, and K. G. Brown, *J. Chem. Phys.* **62**, 1201 (1975).
- [23] A. Sinnock and B. Smith, *Phys. Rev.* **181**, 1297 (1969).
- [24] R. Hahn, T. Battard, O. Boucher, Y. J. Picard, H. Lignier, D. Comparat, N.-A. Keriell, C. Lopez, E. Oswald, M. Reveillard, and M. Viteau, *Rev. Sci. Instrum.* **93**, 043302 (2022).
- [25] D. A. Steck, Cesium D line data, <http://steck.us/alkalidata> (2023).
- [26] S. A. Nepijko, I. Rabin, and W. Schulze, *ChemPhysChem* **6**, 235 (2005).
- [27] J. D. Patterson and B. C. Bailey, *Solid-State Physics: Introduction to the Theory*, 3rd ed. (Springer International Publishing AG, Cham, 2018).
- [28] B. Smith, *Contemp. Phys.* **11**, 125 (1970).
- [29] J. A. Venables and B. L. Smith, *Rare Gas Solids* Vol. II (Academic Press, London, 1977).
- [30] S. Kovalenko and N. Bagrov, *Soviet Phys. Solid State USSR* **11**, 2207 (1970).
- [31] J. Shakhsemampour, R. Pyzalski, M. Vala, and J.-C. Rivoal, *J. Phys.* **45**, 953 (1984).
- [32] K. S. Song and R. T. Williams, *Self-Trapped Excitons*, Springer Series in Solid-State Sciences (Springer-Verlag, Berlin, Heidelberg, 1993).
- [33] W. Schulze and D. Kolb, *J. Chem. Soc. Faraday Trans. 2* **70**, 1098 (1974).
- [34] G. L. Pollack, *Rev. Mod. Phys.* **36**, 748 (1964).
- [35] Y. K. Tovbin, S. Titov, and V. Komarov, *Phys. Solid State* **57**, 360 (2015).
- [36] Y. K. Tovbin, V. Komarov, and E. Gvozdeva, *Prot. Met. Phys. Chem. Surf.* **53**, 591 (2017).
- [37] N. Tishchenko, *Phys. Stat. Sol. A* **73**, 279 (1982).
- [38] N. Tishchenko, *Phys. Stat. Sol. A* **83**, 513 (1984).
- [39] I. V. Leibin, I. S. Kalinina, D. S. Bezrukov, and A. A. Buchachenko, *J. Chem. Phys.* **154**, 044305 (2021).
- [40] L. Blank, D. E. Weeks, and G. S. Kedziora, *J. Chem. Phys.* **136**, 124315 (2012).
- [41] T. Kobayashi, K. Yuki, and L. Matsuoka, *Chem. Lett.* **45**, 1400 (2016).
- [42] A. A. Medvedev, V. V. Meshkov, A. V. Stolyarov, and M. C. Heaven, *Phys. Chem. Chem. Phys.* **20**, 25974 (2018).
- [43] G. K. Ozerov, D. S. Bezrukov, and A. A. Buchachenko, *Low Temp. Phys.* **45**, 301 (2019).
- [44] N. N. Kleshchina, I. S. Kalinina, I. V. Leibin, D. S. Bezrukov, and A. A. Buchachenko, *J. Chem. Phys.* **151**, 121104 (2019).
- [45] U. K. Deiters and R. J. Sadus, *J. Chem. Phys.* **150**, 134504 (2019).
- [46] V. F. Lotrich and K. Szalewicz, *Phys. Rev. Lett.* **79**, 1301 (1997).

- [47] P. Schwerdtfeger, R. Tonner, G. E. Moyano, and E. Pahl, *Angew. Chem. Int. Ed.* **55**, 12200 (2016).
- [48] D. Bezrukov, N. Kleshchina, I. Kalinina, and A. Buchachenko, *Russ. J. Phys. Chem.* **93**, 1505 (2019).
- [49] M. Lara-Moreno, J. Alvarez-Hernández, H. Negrín-Yuvero, J. G. McCaffrey, and G. Rojas-Lorenzo, *Low Temp. Phys.* **45**, 697 (2019).
- [50] N. N. Kleshchina, K. A. Korchagina, D. S. Bezrukov, and A. A. Buchachenko, *J. Phys. Chem. A* **121**, 2429 (2017).
- [51] L.-G. Tao, N. N. Kleshchina, R. Lambo, A. A. Buchachenko, X.-G. Zhou, D. S. Bezrukov, and S.-M. Hu, *J. Chem. Phys.* **143**, 174306 (2015).
- [52] N. Lam, N. Doan, and L. Dagens, *J. Phys. F: Met. Phys.* **15**, 799 (1985).
- [53] N. Lam and L. Dagens, *J. Phys. F: Met. Phys.* **16**, 1373 (1986).
- [54] M. Sabochick, S. Yip, and N. Lam, *J. Phys. F: Met. Phys.* **18**, 349 (1988).
- [55] H. Zenia, K. Lounis, E. Megchiche, and C. Mijoule, *Comput. Mater. Sci.* **124**, 428 (2016).
- [56] K. Lounis, H. Zenia, E. Megchiche, and C. Mijoule, *Comput. Mater. Sci.* **118**, 279 (2016).
- [57] R. M. J. Cotterill and M. Doyama, *Calculation of the Properties of Vacancies and Interstitials: Proceedings* (US Department of Commerce, National Bureau of Standards, Shenandoah National Park, Virginia, 1966), Vol. 13, p. 47.
- [58] A. Damask, *Science* **162**, 448 (1968).
- [59] R. Johnson, *J. Phys. F: Met. Phys.* **3**, 295 (1973).
- [60] L. Y. Nemirovich-Danchenko, A. Lipnitskiui, and S. Kul'kova, *Phys. Solid State* **49**, 1079 (2007).
- [61] H. Wang, D. Rodney, D. Xu, R. Yang, and P. Veysseyre, *Philos. Mag.* **93**, 186 (2013).
- [62] J. Peng, S. Bahl, A. Shyam, J. A. Haynes, and D. Shin, *Acta Mater.* **196**, 747 (2020).
- [63] We use the following articles [49,52–62] and using their notations; these include, for instance, for zero-vacancy octahedral, tetrahedral, crowdion and $\langle 100 \rangle$, $\langle 110 \rangle$, and $\langle 111 \rangle$ interstitial sites; for one vacancy cornered or centered substitutional sites; for two vacancies corner to center (2v-a) to corner (2v-b) or to tetrahedral (2v-c) sites; for three vacancies corner to center-center (3v-a) to corner-center (3v-b) to center-corner (3v-c: linear) sites; for four vacancies tetrahedral, rhombic or squared; the five, seven, and eight vacancies are typically taken from the six-vacancy plus (or minus) centered, tetraedral, or corner sites.
- [64] D. P. Kingma and J. Ba, *Proceedings of the 3rd International Conference on Learning Representations, San Diego, CA, USA* (ICLR, 2015).
- [65] T. Dozat, Incorporating nesterov momentum into adam (2016).
- [66] S. Ruder, [arXiv:1609.04747](https://arxiv.org/abs/1609.04747).
- [67] S. H. Haji and A. M. Abdulazeez, *PalArch's J. Archaeol. Egypt/Egyptol.* **18**, 2715 (2021).
- [68] J. Simons, *An Introduction to Theoretical Chemistry* (Cambridge University Press, 2003).
- [69] M. Heaven and A. Stolyarov, *Proceedings of the 41st Plasma-dynamics and Lasers Conference* (Chicago, Illinois, 2010), p. 4877.
- [70] M. Ryan, M. Collier, P. d. Pujó, C. Crépin, and J. G. McCaffrey, *J. Phys. Chem. A* **114**, 3011 (2010).
- [71] E. Jacquet, D. Zanuttini, J. Douady, E. Giglio, and B. Gervais, *J. Chem. Phys.* **135**, 174503 (2011).
- [72] M. Diaz Peña, C. Pando, and J. Renuncio, *J. Chem. Phys.* **73**, 1750 (1980).
- [73] S. Dridi, M. B. Amar, M. Abderraba, and J.-P. Passarello, *Fluid Phase Equilib.* **562**, 113563 (2022).
- [74] H. Stenschke, *J. Chem. Phys.* **100**, 4704 (1994).
- [75] B. B. Akhouri and J. R. Solana, *Physica A: Stat. Mech Applic.* **608**, 128280 (2022).
- [76] H. Berendsen, *Simulating the Physical World* (Cambridge University Press, New York, 2007).
- [77] P. Ströker, R. Hellmann, and K. Meier, *Phys. Rev. E* **105**, 064129 (2022).
- [78] M. Lax, *J. Chem. Phys.* **20**, 1752 (1952).
- [79] E. J. Heller, *J. Chem. Phys.* **68**, 2066 (1978).
- [80] R. S. Mulliken, *J. Chem. Phys.* **55**, 309 (1971).
- [81] J. Tellinghuisen, The Franck-Condon principle, in *Photons and Continuum States of Atoms and Molecules: Proceedings of a Workshop Cortona, Italy, June 16–20, 1986* (Springer, 1987), pp. 149–156.
- [82] L. Barragán-Gil and R. Walser, *Am. J. Phys.* **86**, 22 (2018).
- [83] J. P. Bergsma, P. H. Berens, K. R. Wilson, D. R. Fredkin, and E. J. Heller, *J. Phys. Chem.* **88**, 612 (1984).
- [84] J. A. Boatz and M. E. Fajardo, *J. Chem. Phys.* **101**, 3472 (1994).
- [85] E. Pavarini, E. Koch, F. Anders, and M. Jarrell, *Correlated Electrons: From Models to Materials Modeling and Simulation* (Forschungszentrum Jülich, 2012), Chap. 6, Vol. 2.
- [86] B. S. Tsukerblat, *Group Theory in Chemistry and Spectroscopy: A Simple Guide to Advanced Usage* (Academic Press, San Diego, 2006).
- [87] M. S. Dresselhaus, G. Dresselhaus, and A. Jorio, *Group Theory: Application to the Physics of Condensed Matter* (Springer-Verlag, Berlin, Heidelberg, 2008).
- [88] W. Hergert and R. M. Geilhufe, *Group Theory in Solid State Physics and Photonics: Problem Solving with Mathematica* (Wiley-VCH, 2018).
- [89] J. Van Vleck, *J. Chem. Phys.* **7**, 72 (1939).
- [90] Y. Toyozawa and M. Inoue, *J. Phys. Soc. Jpn.* **21**, 1663 (1966).
- [91] K. Cho, *J. Phys. Soc. Jpn.* **25**, 1372 (1968).
- [92] P. Lund, D. Smith, S. Jacobs, and P. Schatz, *J. Chem. Phys.* **88**, 31 (1984).
- [93] J. Ammeter and D. Schlosnagle, *J. Chem. Phys.* **59**, 4784 (1973).
- [94] I. Bersuker, *Coord. Chem. Rev.* **14**, 357 (1975).
- [95] F. Forstmann, D. Kolb, D. Leutloff, and W. Schulze, *J. Chem. Phys.* **66**, 2806 (1977).
- [96] D. Kolb, D. Leutloff, W. Schulze, and F. Forstmann, *Ber. Bunsenges. Phys. Chem.* **82**, 33 (1978).
- [97] M. O'Brien, *J. Phys. C: Solid State Phys.* **4**, 2524 (1971).
- [98] H.-J. Stöckmann, *Z. Phys. B* **54**, 229 (1984).
- [99] I. B. Bersuker, *The Jahn-Teller Effect and Vibronic Interactions in Modern Chemistry*, Mechanics: Genesis and Method (Springer Science & Business Media, New York, 1984).
- [100] M. Jakob, H. Micklitz, and K. Luchner, *Phys. Lett. A* **57**, 67 (1976).
- [101] M. Jakob, H. Micklitz, and K. Luchner, *Phys. Lett. A* **61**, 265 (1977).
- [102] K. Luchner and H. Micklitz, *J. Lumin.* **18–19**, 882 (1979).
- [103] R. Lambo, A. A. Buchachenko, L. Wu, Y. Tan, J. Wang, Y. R. Sun, A.-W. Liu, and S.-M. Hu, *J. Chem. Phys.* **137**, 204315 (2012).

- [104] R. Lambo, C.-Y. Xu, S. T. Pratt, H. Xu, J. C. Zappala, K. G. Bailey, Z.-T. Lu, P. Mueller, T. P. O'Connor, B. B. Kamorzin *et al.*, *Phys. Rev. A* **104**, 062809 (2021).
- [105] M. Wagner, *J. Chem. Phys.* **41**, 3939 (1964).
- [106] T. H. Keil, *Phys. Rev.* **140**, A601 (1965).
- [107] X. Shi-Jie, *Acta Phys. Sin* **68** (2019).
- [108] Y. Zhang, *J. Semicond.* **40**, 091102 (2019).
- [109] M. Sturge, in *The Jahn-Teller Effect in Solids*, edited by F. Seitz, D. Turnbull, and H. Ehrenreich, Solid State Physics Vol. 20 (Academic Press, 1968), pp. 91–211.
- [110] C. A. Bates, *Phys. Rep.* **35**, 187 (1978).
- [111] C. Bates, J. Dunn, and E. Sigmund, *J. Phys. C: Solid State Phys.* **20**, 1965 (1987).
- [112] M. O'Brien and S. Evangelou, *J. Phys. C: Solid State Phys.* **13**, 611 (1980).
- [113] J. Rose, D. Smith, B. Williamson, P. Schatz, and M. O'Brien, *J. Phys. Chem.* **90**, 2608 (1986).
- [114] B. Hüpper and B. Eckhardt, *Phys. Rev. A* **57**, 1536 (1998).
- [115] O. Anatole von Lilienfeld and A. Tkatchenko, *J. Chem. Phys.* **132**, 234109 (2010).
- [116] M. Groß and F. Spiegelmann, *Eur. Phys. J. D* **4**, 219 (1998).
- [117] J. D. Hewitt, C. Campbell, K. T. Raymond, S. Park, K. V. Desai, A. E. Mironov, and J. G. Eden, *J. Phys. Chem. A* **127**, 3675 (2023).
- [118] R. A. Corbin and M. E. Fajardo, *J. Chem. Phys.* **101**, 2678 (1994).
- [119] S. L. Laursen and H. E. Cartland, *J. Chem. Phys.* **95**, 4751 (1991).
- [120] M. Guarise, *Eur. Phys. J. Plus* **137**, 1 (2022).
- [121] R. L. Lambo, G. K. Koyanagi, A. Ragyanszki, M. Horbatsch, R. Fournier, and E. A. Hessels, *Mol. Phys.* **121**, e2198044 (2023).
- [122] G. K. Koyanagi, R. L. Lambo, A. Ragyanszki, R. Fournier, M. Horbatsch, E. A. Hessels, and EDM3 collaboration, *J. Mol. Spectr.* **391**, 111736 (2023).
- [123] R. M. Geilhufe and W. Hergert, *Front. Phys.* **6**, 86 (2018).
- [124] A. F. Devonshire, *Proc. Roy. Soc. London A* **153**, 601 (1936).
- [125] S. K. Misra, H. A. Buckmaster, E. Reijerse, S. Subramanian, and M. C. Krishna, *Multifrequency Electron Paramagnetic Resonance* (John Wiley & Sons, Hoboken, NJ, 2011), Chap. 4, pp. 115–228.
- [126] I. D. Ryabov, *Appl. Magn. Reson.* **35**, 481 (2009).
- [127] C. D. Lewis and D. E. Weeks, *J. Phys. Chem. A* **121**, 3340 (2017).
- [128] D. Varshalovich, A. Moskalev, and V. Khersonskii, *Quantum Theory of Angular Momentum* (World Scientific, Singapore, 1988).
- [129] P. P. Man, *Concepts Magnet. Resonance A* **45A**, e21385 (2016).
- [130] J. W. Kenney III, J. A. Boatz, and H. A. Terrill Vosbein, *Int. J. Quantum Chem.* **103**, 854 (2005).
- [131] U. Hergenbahn, *J. Phys. B* **37**, R89 (2004).
- [132] W. Siebrand, *J. Chem. Phys.* **46**, 440 (1967).
- [133] K. F. Freed and S. Lin, *Chem. Phys.* **11**, 409 (1975).
- [134] E. J. Heller, *J. Chem. Phys.* **65**, 1289 (1976).
- [135] S. Mukamel, *J. Chem. Phys.* **77**, 173 (1982).
- [136] J. Shao, J.-L. Liao, and E. Pollak, *J. Chem. Phys.* **108**, 9711 (1998).
- [137] I. M. Ansari, E. R. Heller, G. Trenins, and J. O. Richardson, *Philos. Trans. R. Soc. A* **380**, 20200378 (2022).
- [138] E. Wigner, *Phys. Rev.* **40**, 749 (1932).
- [139] V. Tatarskiĭ, *Soviet Phys. Uspekhi* **26**, 311 (1983).
- [140] M. Hillery, R. F. O'Connell, M. O. Scully, and E. P. Wigner, *Phys. Rep.* **106**, 121 (1984).
- [141] W. B. Case, *Am. J. Phys.* **76**, 937 (2008).
- [142] D. K. Ferry and M. Nedjalkov, *The Wigner Function in Science and Technology* (IoP Publishing, 2018).
- [143] B. Segev, *J. Opt. B* **5**, S381 (2003).
- [144] Y. Japha and B. Segev, *Phys. Rev. A* **65**, 063411 (2002).
- [145] A. Sergeev and B. Segev, *J. Chem. Phys.* **118**, 5852 (2003).
- [146] E. Pollak and J. Cao, *Phys. Rev. A* **107**, 022203 (2023).
- [147] S. Kallush, B. Segev, A. Sergeev, and E. Heller, *J. Phys. Chem. A* **106**, 6006 (2002).
- [148] B. Segev and A. Sergeev, *Chem. Phys. Lett.* **367**, 382 (2003).
- [149] E. R. Heller and J. O. Richardson, *J. Chem. Phys.* **152**, 244117 (2020).
- [150] F. Agostini and B. F. Curchod, *Philos. Trans. Roy. Soc. A* **380**, 20200375 (2023).
- [151] R. Bell, *J. Phys. B: At. Mol. Phys.* **3**, 751 (1970).
- [152] Y. Midzuno and T. Kihara, *J. Phys. Soc. Jpn.* **11**, 1045 (1956).
- [153] B. Axilrod and E. Teller, *J. Chem. Phys.* **11**, 299 (1943).
- [154] Y. Mutô, *Nippon Sugaku-Buturigakkwaishi* **17**, 629 (1943).
- [155] M. Lepers and O. Dulieu, *Phys. Chem. Chem. Phys.* **13**, 19106 (2011).
- [156] P.-G. Yan, L.-Y. Tang, Z.-C. Yan, and J. F. Babb, *Phys. Rev. A* **104**, 022807 (2021).
- [157] M. H. Muser, S. V. Sukhomlinov, and L. Pastewka, *Adv. Phys.: X* **8**, 2093129 (2023).
- [158] S. Grimme, A. Hansen, J. G. Brandenburg, and C. Bannwarth, *Chem. Rev.* **116**, 5105 (2016).
- [159] P. Xu, M. Alkan, and M. S. Gordon, *Chem. Rev.* **120**, 12343 (2020).
- [160] U. K. Deiters and R. J. Sadus, *J. Phys. Chem. B* **125**, 8522 (2021).
- [161] R. J. Le Roy, *Can. J. Phys.* **52**, 246 (1974).
- [162] J. Kielkopf, *J. Chem. Phys.* **61**, 4733 (1974).
- [163] K. Tang, *Phys. Rev.* **177**, 108 (1969).
- [164] T. Gould and T. Bucko, *J. Chem. Theory Comput.* **12**, 3603 (2016).
- [165] R. Bell and A. Kingston, *Proc. Phys. Soc.* **88**, 901 (1966).
- [166] B. Bussery, M. Aubert-Frécon, and M. Saute, *Chem. Phys.* **109**, 39 (1986).
- [167] J.-Y. Zhang and J. Mitroy, *Phys. Rev. A* **76**, 022705 (2007).